REVISTA MATÉRIA V.31
ISSN 1517-7076 articles e20250940, 2026

# Mechanical response and damage metrics across polymer- and metal-matrix composites: CFRP and AA7065–$B_4C$–graphite hybrid MMC

Madhan Arumugam Baladhandapani[1], Parthiban Alagesan[1]

[1] Vels Institute of Science, Technology & Advanced Studies, Department of Mechanical Engineering. Tamil Nadu, India.
e-mail: madhanbaladhandapani@gmail.com, parthibana83@gmail.com

## ABSTRACT

Unidirectional carbon/epoxy laminates form the basis of weight-sensitive structures, yet tensile allowables depend on strain metrology and fiber-orientation traceability. A locked tensile workflow that removes compliance bias and enforces channel synchronization for orientation-resolved property extraction has not been previously reported. This study develops a compliance-aware, time-synchronized tensile evaluation for 0°, 45°, and 90° coupons taken from a single 16 panel. A 16-ply laminate with fiber volume fraction near 55% was fabricated. Coupons were tabbed and tested quasi-statically with extensometry, crosshead records were corrected by rigid-coupon calibration, and strength scatter was modeled using two-parameter Weibull statistics with bootstrap uncertainty for energy metrics. Anisotropy is large: the 0° modulus was 66.6–66.7 GPa and strength was ~800 MPa, the 45° modulus was ~15.0 GPa with ~150 MPa strength and ~3.0% failure strain, and the 90° modulus was 3.3–3.36 GPa with ~50 MPa strength. Energy absorption is orientation dependent; strain-energy density to failure was 4.59 MJ $m^{-3}$ at 0°, 3.50 MJ $m^{-3}$ at 45°, and 0.36 MJ $m^{-3}$ at 90°. The processing chain yields design-ready properties and reliability descriptors suitable for lamina-level modeling and combined-stress assessment. Future work targets hygrothermal conditioning, full-field strain mapping, and strain-rate coverage from $10^{-5}$ to $10^{-1}$ $s^{-1}$.

**Keywords:** CFRP laminate; Tensile testing; Fiber orientation; Modulus extraction; Strain localization.

## 1. INTRODUCTION

Lightweight structural design increasingly depends on materials whose performance is governed as much by measurement fidelity as by intrinsic strength. Unidirectional carbon fiber–reinforced polymer (CFRP) laminates enable high specific stiffness and strength in aircraft structures, wind-turbine blades, and other weight-sensitive systems, yet their tensile response remains strongly orientation dependent. The balance between fiber-dominated axial load transfer and matrix-dominated transverse and shear deformation shifts with small changes in fiber angle, and that shift alters stiffness, strength, energy absorption, and failure morphology [1]. Reliable tensile characterization across principal orientations therefore remains a central requirement for laminate sizing, constitutive calibration, and allowable development.

Accepted lamina mechanics provides the framework used to interpret this anisotropy. Under plane stress, an applied axial state is resolved into lamina components $\sigma_{11}$, $\sigma_{22}$, and $\tau_{12}$ through standard transformation relations, and those components are routinely used for off-axis interpretation and laminate-level modelling [2]. Combined-stress assessment in composite design commonly relies on quadratic interaction criteria, including Tsai–Hill and Tsai–Wu, because mixed-mode stress components arise naturally in angled plies and off-axis tensile coupons. Off-axis tension is also used to probe shear-governed deformation in unidirectional systems because coupling between axial loading and in-plane shear is introduced in the material coordinate system. As a consequence, tensile data from 0°, 45°, and 90° coupon sets is commonly used as a baseline input for failure checks, envelope construction, and model validation [3].

Current research trends (Table 1) indicate linking composite performance to controllable levers that span manufacturing, service environment, and interface quality, while coupling mechanical tests to sensing and mechanistic modeling. Stacking architecture and consolidation conditions are treated as structural design parameters that shape anisotropy, delamination propensity, and machining robustness. Conditioning studies extend these dependencies into operational regimes, demanding workflows that preserve metrological fidelity when stiffness

Corresponding Author: Madhan Arumugam Baladhandapani Received on 01/11/2025 Accepted on 11/02/2026

DOI: https://doi.org/10.1590/1517-7076-RMAT-2025-0940

**Table 1:** Composite-property drivers spanning environment, processing, interfacial tailoring.

| METHODOLOGY/ APPROACH | MATERIALS/ PARAMETERS STUDIED | KEY FINDINGS/ RESULTS | RELEVANCE TO CURRENT STUDY |
|---|---|---|---|
| Vacuum bagging; Charpy; 3D FE; Hashin+CZM | UD CFRP/GFRP/hybrids; RT to −196°C; 0°/90° | Δ Hybrid energy; temperature shifts damage; FE validated | Cryogenic conditioning path for tensile protocol extension [4] |
| Drilling; force/torque; roughness; hole damage | Al2024/FRP/Al2024; glass/ carbon; stacks; cutting parameters | Δ Force carbon; Δ torque glass; Δ roughness all-glass | Metrology control for machining-induced bias versus orientation [5] |
| Tube tests; drilling; thrust and damage metrics | BFRP pipes; [±30/±60/±90]3 sequences | Δ Mechanics with ±90 placement; Δ drilling thrust | Reinforces stacking/ orientation traceability in datasets [6] |
| Ring tensile; drilling; delamination/roughness; backup | FW hybrids; GGC/GCG/CGG; cutting; backup use | Δ Delamination with backup; ∇ roughness 9–40% | Fixture/backup effects relevant to coupon preparation quality [7] |
| Nanofilled epoxy; DSC/ TGA/FTIR; tensile/ flexural; SEM | Epoxy 0.5–4 wt.% α-Fe2O3; GFRC laminates | Δ Strength 13.62%; Δ toughness 37.94%; ∇ flexural 20.54% | Matrix tuning influences tensile metrics and failure modes [8] |
| Heat exposure; tensile; DMA/DSC/TGA; burn-off; tanh model | Pultruded GFRP; 80–400°C; 15–45 min | Δ Post-cure at 80°C; ∇ strength 41.3% at 400°C | Temperature-conditioning extension with compliance-consistent tracking [9] |
| Plasma activation; tensile/fracture; in-situ AE; SEM/XPS | CF/epoxy; APA duration series | Δ Strength 13.5%; Δ GIc 53%; Δ GIIc 44% | Interface strengthening; AE damage monitoring integration [10] |
| TAI at −55°C; 10 J BVID; AE; fractography | CF/epoxy joints; HBB vs OB; CP/AP | ∇ TAI capacity; Δ brittleness at −55°C; mode shift | Low-temperature damage tolerance informs protocol expansions [11] |
| AFP; 300/600 N; tensile; DCB/ENF/SBS; AE | UD/CP/QI CFRP; compaction force | Δ QI strength 12%; Δ Mode-I 16%; AE metrics | Process-variable control and AE inclusion rationale [12] |
| Ring tensile; drilling; delamination/roughness; thrust | FW GFRP; ±55°; cutting; backup materials | ∇ Delamination with backup; ∇ roughness; Δ thrust | Boundary-condition effects on measured responses [13] |
| LT/HT/CHT; DCB+AE; ENF; SBS; 3PB; microscopy | UD CF/PEKK; low/high T; cyclic hygrothermal | Δ ILSS LT; ∇ flexural HT; ∇ toughness CHT | Environmental roadmap beyond room-temperature tensile baselines [14] |

and failure evolve. This motivates compliance-aware, synchronization-controlled tensile characterization that isolates material response from system artifacts while supplying damage and reliability descriptors suitable for design allowables and model calibration.

Despite this mature mechanics basis, published unidirectional CFRP tensile datasets were often constrained by ambiguities rooted in metrology and processing choices rather than in fundamental theory. Coupon orientation was sometimes reported without an explicit datum, tolerance, and extraction map, even though small angular deviations can shift measured response when matrix shear contributes significantly. Early-slope estimates were also biased when machine and grip compliance was embedded in displacement records, particularly when crosshead displacement was substituted for gauge strain. Extensometer handling created additional discontinuities, because extensometers were frequently removed before final fracture in fiber-aligned tests, leaving a partial strain record that required reconstruction [15]. Tabbing, gripping pressure, and friction conditions further influenced boundary conditions and failure location, and failure was occasionally steered outside the gauge when those conditions varied across specimens.

Data integrity and reduction practices also introduced variability that limited direct reuse of tensile records for modeling and reliability tasks. Force and strain channels were not consistently synchronized, even though acquisition latency and filtering can introduce small time offsets that distort slope-based calculations and derivative measures. Modulus was extracted using differing strain windows, and curve truncation near

failure was handled inconsistently across studies, which complicated comparisons across orientations. Energy metrics, when reported, were not always computed using a consistent numerical procedure, and derivative descriptors intended to track stiffness evolution were sensitive to noise, alignment, and smoothing choices [16]. These issues reduced the portability of tensile data into orientation-resolved design artifacts, including stress-component checks derived from lamina transformations and combined-stress utilization evaluated by Tsai–Hill or Tsai–Wu formulations.

A research gap was therefore defined by the need for an end-to-end tensile evaluation workflow for unidirectional CFRP that preserved orientation traceability, removed compliance-induced bias from strain measurement, enforced time-base alignment of channels, and fixed the data-reduction steps before batch processing [17]. That need was not met by listing routine laboratory controls as novelty, because panel fabrication consistency, orientation mapping, and standard instrument calibration represent credibility safeguards expected in competent tensile testing. Instead, methodological novelty was required at the measurement–analysis interface, where strain continuity had to be preserved when extensometer coverage was incomplete, where compliance effects had to be quantified and removed, and where synchronization and processing definitions had to be locked so that derivative and energy quantities were not tuned specimen by specimen [18].

The present work was structured to address this gap using a controlled unidirectional carbon/epoxy laminate and a compliance-aware, synchronization-enforced processing framework. A single laminate panel was used as a shared material baseline for 0°, 45°, and 90° coupons, and an explicit extraction convention with a stated angular tolerance was applied to prevent ambiguity in orientation assignment; these elements were treated as experimental controls that supported comparability [19]. Methodological additions were concentrated in the construction of a hybrid strain history and in a fixed reduction pipeline. Machine compliance was quantified using a rigid calibration specimen under matched gripping conditions, and compliance-corrected crosshead displacement was integrated with extensometer strain to preserve a continuous gauge-level strain record when extensometer removal was required. Time-base alignment between force and strain was enforced through cross-correlation so that regression-based modulus extraction, numerical integration for energy metrics, and derivative calculations for stiffness-change descriptors were computed from synchronized arrays [20]. Reliability descriptors were incorporated through Weibull modeling of ultimate strength within each orientation group so that scatter could be reported as distribution parameters suited to allowable development.

Transferability beyond polymer composites was also required if the workflow was to function as a general validation template for structural materials. For that purpose, a second phase was implemented on an AA7065–$B_4C$–graphite hybrid metal matrix composite, where microstructure- and processing-induced variability differs from that of unidirectional CFRP. Three replicate specimens were tested as a pilot set to establish baseline repeatability and to screen fabrication- and preparation-induced variability under the same measurement logic and reduction template [21]. The pilot replication was used to validate the processing chain under a distinct failure and deformation regime and to inform subsequent expansion of replicate count in later phases when statistics across conditions are required.

Accordingly, the objective of this study was to conduct an orientation-controlled tensile campaign on unidirectional carbon/epoxy coupons at 0°, 45°, and 90° using compliance-aware and time-synchronized strain measurement, to execute a locked data-reduction workflow that yields reproducible properties, energy metrics, stiffness-change descriptors, and reliability parameters compatible with lamina transformations and Tsai–Hill/Tsai–Wu assessment, and to demonstrate methodological transferability through a pilot three-specimen tensile evaluation of an AA7065–$B_4C$–graphite hybrid metal matrix composite.

## 2. MATERIALS AND METHODS

A unidirectional carbon-fiber/epoxy prepreg was used as the sole feedstock for laminate fabrication. Frozen storage was maintained at –18°C in sealed foil packaging with desiccant, and thawing was performed while sealed for 2 h at 25 ± 2°C to limit condensation. Layup was performed in an air-conditioned laboratory in Chennai, Tamil Nadu, India, with ambient conditions recorded as 25 ± 2°C and 60 ± 10% relative humidity, and cumulative out-time was tracked and recorded. All identifiers, handling history, and cure schedule parameters required for reproducibility were listed in Table 2 at first mention so that the material state underlying each specimen was defined explicitly.

Figure 1 illustrates the specimen-production sequence from prepreg feedstock to cured panel, and the schematic was used to define each fabrication stage, the order of operations, and the boundary conditions applied during consolidation. The prepreg was cut into plies using a straightedge aligned to the supplier fiber-direction tracer so that a single fiber-axis datum was preserved through stacking. $A[0]_{16}$ laminate was assembled by hand on a polished steel tool plate that was degreased with isopropyl alcohol and coated with a non-silicone

**Table 2:** Prepreg identification, constituent specifications, storage history, and cure schedule recorded for reproducibility (Chennai laboratory conditions).

| CATEGORY | PARAMETER | RECORDED VALUE | UNIT/NOTE |
|---|---|---|---|
| Storage condition | Frozen storage setpoint | −18 | °C |
| Storage condition | Packaging state | Sealed foil pouch with desiccant | moisture barrier |
| Handling history | Thaw condition | 2 | h at 25 ± 2°C (*sealed*) |
| Handling history | Layup environment | 25 ± 2°C; 60 ± 10 | lab record |
| Handling history | Cumulative out-time | 6 | h at 27 ± 2°C (tracked) |
| Recommended cure | Supplier recommended cycle | Ramp → 120°C; dwell 2 h; controlled cool | add ramp/cool rates if supplied |
| Applied cure (actual) | Platen pressure | 0.5 | MPa |
| Applied cure (actual) | Peak temperature | 120 | °C |
| Applied cure (actual) | Dwell time | 2 | h |
| Applied cure (actual) | Cool-down condition | Controlled to ambient under pressure | hot-press execution |

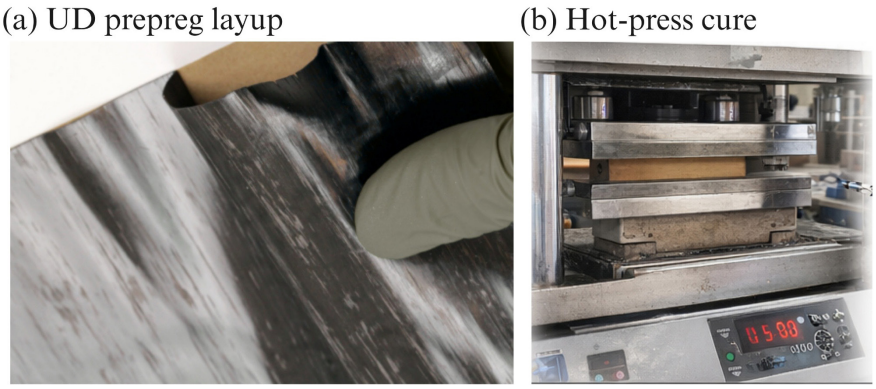


**Figure 1:** (a) UD preparation; (b) hot press cure.

release system, and ply edges were registered to tool marks to maintain a consistent panel datum. The stack was consolidated in a hot press using nonporous release films and caul plates to promote uniform pressure transfer, and a controlled ramp–dwell–cool schedule was applied under constant platen pressure of 0.5 MPa, with a dwell at 120°C for 2 h and a controlled cool-down under pressure. Panel planform was set to 300 mm × 300 mm, and laminate thickness $t_L$(mm) was measured at multiple locations to record thickness variability for downstream geometry normalization. Nominal cured ply thickness $t_p$(mm) was calculated from $t_L$ and ply count $N_p$ = 16 as expressed in Equation 1, and the variables $t_L$(mm), $N_p$(–), and $t_p$(mm) were defined at first use.

$$t_p = \frac{t_L}{N_p} \tag{1}$$

Constituent fraction was documented using a resin burn-off protocol applied to trimmed perimeter segments taken from the cured panel. The initial specimen mass $m_0$(g) was recorded, the matrix was removed under controlled heating until mass stabilized, and the remaining fiber mass $m_f$(g) was recorded after cooling in a desiccator. Fiber mass fraction $w_f$(–) was calculated as expressed in Equation 2, and $m_0$(g), $m_f$(g), and $w_f$(–) were defined immediately after first appearance.

$$w_f = \frac{m_f}{m_0} \tag{2}$$

Fiber volume fraction $V_f$(–) was estimated using supplier-reported densities $\rho_f$(g cm$^{-3}$) and $\rho_m$ (g cm$^{-3}$) for fiber and cured resin, using Equation 3, and $\rho_f$, $\rho_m$, and $V_f$ were defined at first use.

$$V_f = \frac{w_f/\rho_f}{(w_f/\rho_f)+[(1-w_f)/\rho_m]} \tag{3}$$

Figure 2 shows the orientation-controlled coupon extraction map, and the schematic was used to define the fiber-axis datum, the coupon long-axis definition for each target orientation, and the angular tolerance band applied during cutting. Coupons were extracted at nominal orientations of 0°, 45°, and 90° relative to the original fiber axis marked on the panel. Centerlines were drawn using a datum edge and an angle template, and each centerline was constrained within ±0.5° of the intended direction by verification against the template prior to cutting. Cutting was performed using a water-cooled diamond saw, and the panel was clamped to a sacrificial backing board to suppress exit-side splintering. Edge dressing was performed using fine abrasive paper with strokes parallel to the local fiber direction to remove loose splinters without fiber buckling. Coupons with visible edge splitting, delamination at the cut edge, or angular deviation beyond tolerance were rejected prior to tabbing and were replaced so that the replication plan remained fixed.

Figure 3 presents the standardized coupon geometry, and the schematic was used to define the gauge region, the tabbed grip regions, and the dimensional basis used for stress and strain reduction. Each coupon was machined to total length $L$ = 250 mm and width $b$ = 25 mm, with a centered gauge length $L_g$ = 150 mm and tab lengths of 50 mm at each end. Thickness $t$(mm) and width $b$(mm) were measured at three positions along the gauge using a calibrated digital caliper with 0.01 mm resolution, and the mean values were used to calculate initial cross-sectional area $A_0$(mm$^{-2}$) as expressed in Equation 4, with $b$(mm), $t$(mm), and $A_0$(mm$^{-2}$) defined immediately after first appearance.

$$A_0 = b\,t \tag{4}$$

End tabs were bonded to reduce grip-induced damage and to stabilize load transfer. Tabs were cut from a glass/epoxy sheet of nominal thickness 1.5 mm, machined to 50 mm length, and chamfered at 10–15° to reduce peel stress at the tab termination. Bonding surfaces were abraded with 220-grit paper, cleaned with isopropyl alcohol, and dried. A two-part structural epoxy adhesive was mixed by mass ratio according to the supplier's instructions, applied as a thin, continuous film, and cured under a tabbing jig that enforced symmetry and parallelism. Cure was performed at room temperature for 24 h followed by a post-cure at 50–60°C for 2 h to stabilize adhesive stiffness. Tab alignment was verified by measuring tab overhang and gauge centering before testing.

Mechanical testing was performed on an electromechanical universal test machine (Instron 5985, Instron, Norwood, MA, USA) equipped with a 100 kN load cell. Load-cell verification was performed against a traceable standard in accordance with ASTM E4 before the test series, and a zero check was performed immediately

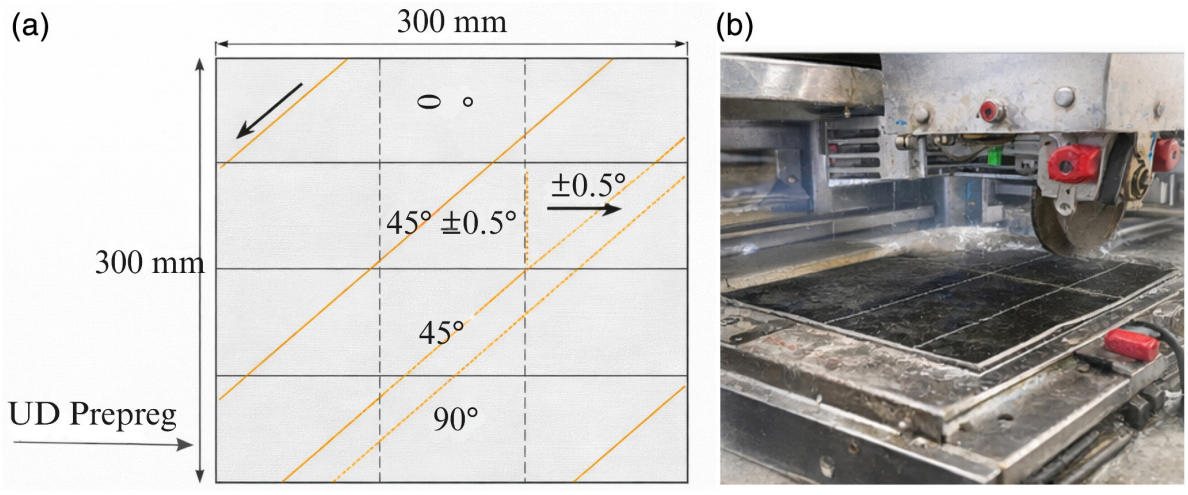


**Figure 2:** Extraction map and angular tolerance used to produce 0°, 45°, and 90° tensile coupons from a single cured panel.

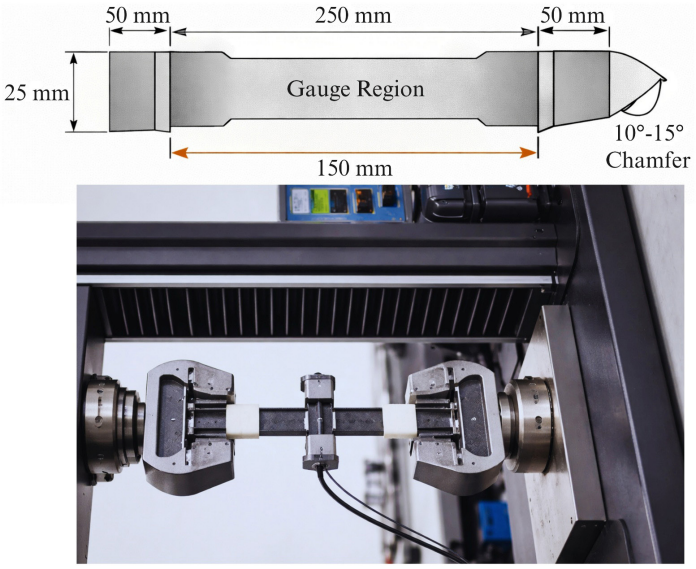


**Figure 3:** Single-panel schematic defining the tensile coupon dimensions, gauge region, tab lengths, and chamfer used for standardized load introduction and metrology.

before each test. Wedge-action grips with serrated steel faces were used, and fine-grit abrasive liners were placed between tab surfaces and grip faces to suppress slip. A clip-on axial extensometer with gauge length $L_e$ = 50 mm was attached at the gauge center, and calibration was verified using a certified reference block. Crosshead speed was set to 2 mm min$^{-1}$, and acquisition of force $F$(N), crosshead displacement $\delta$(mm), and extensometer strain $\varepsilon_e$(–) was performed at sampling frequency $f_s$ = 50 Hz. Equipment identifiers, acquisition settings, and boundary-condition parameters were documented in Table 3 at first mention.

A compliance correction was implemented to support strain reconstruction when the extensometer was removed prior to terminal fracture. A rigid dummy coupon with negligible axial strain in the working load range was loaded under the same grip condition and crosshead control, and machine stiffness $k_m$(N mm$^{-1}$) was estimated by an origin-constrained least-squares fit as expressed in Equation 5, with $F_j$(N) and $\delta_j$(mm) denoting the $j$-th sampled force and displacement pair and $N$(–) denoting the number of samples used in the fit.

$$k_m = \frac{\sum_{j=1}^{N} \delta_j F_j}{\sum_{j=1}^{N} \delta_j^2} \tag{5}$$

Machine compliance $C_m$(mm N$^{-1}$) was defined as the inverse of stiffness as expressed in Equation 6, and $k_m$ and $C_m$ were defined at first use.

**Table 3:** Test system, sensors, and acquisition parameters used for tensile loading.

| ITEM | SPECIFICATION | RECORDED SETTING |
|---|---|---|
| Test frame | Instron 5985 (Instron, Norwood, MA, USA) | Electromechanical |
| Load cell | 100 kN | Verified to ASTM E4 prior to series |
| Grips | Wedge-action, serrated faces | Abrasive liners at tab interface |
| Extensometer | Clip-on axial extensometer | $L_e$ = 50 mm; reference-block verification |
| Control | Crosshead displacement | 2 mm min$^{-1}$ |
| Acquisition | Logged channels | $F$, $\delta$, $\varepsilon_e$ |
| Sampling | Frequency | $f_s$ = 50 Hz |
| Environment | Laboratory ambient | 25 ± 2°C; 60 ± 10% RH |

$$C_m = \frac{1}{k_m} \tag{6}$$

Compliance-corrected displacement $\delta_c$(mm) was computed from crosshead displacement $\delta$(mm) using Equation 7, and compliance-corrected strain surrogate $\varepsilon_c$(–) was computed using the gauge length $L_g$(mm) using Equation 8, with $\delta$, $\delta_c$, and $\varepsilon_c$ defined at first use.

$$\delta_c = \delta - C_m F \tag{7}$$

$$\varepsilon_c = \frac{\delta_c}{L_g} \tag{8}$$

Time alignment between recorded channels was enforced prior to slope-based calculations. A discrete cross-correlation $R_{xy}(k)$(–) between a reference signal $x[i]$(–) and a target signal $y[i]$(–) was computed as expressed in Equation 9, with $k$ denoting integer lag in samples and $N$ denoting record length in samples.

$$R_{xy}(k) = \sum_{i=1}^{N-k} x[i]\, y[i+k] \tag{9}$$

The lag $k^{\backslash *}$ that maximized correlation was selected as expressed in Equation 10, and $k^{\backslash *}$ was defined at first use.

$$k^{\backslash *} = \arg\max_k \; R_{xy}(k) \tag{10}$$

The corresponding time shift $\tau^{\backslash *}$(s) was computed from sampling interval $\Delta t = 1/f_s$ as expressed in Equation 11, and $\tau^{\backslash *}$and $\Delta t$ were defined immediately after first appearance.

$$\tau^{\backslash *} = k^{\backslash *} \Delta t \tag{11}$$

Engineering stress–strain reduction was performed on synchronized records using initial geometry. Engineering stress $\sigma$(MPa) was computed from force $F$(N) and initial area $A_0$(mm$^{-2}$) as expressed in Equation 12, and $\sigma$ was defined at first use.

$$\sigma = \frac{F}{A_0} \tag{12}$$

Engineering strain $\varepsilon$(–) was taken as the extensometer strain $\varepsilon_e$ during extensometer engagement and as the compliance-corrected strain $\varepsilon_c$ after extensometer removal, and continuity was enforced by matching strain offsets at the removal time index. Elastic modulus $E$(GPa) was computed by least-squares regression of $\sigma$ on $\varepsilon$ over a predefined elastic window $[\varepsilon_1, \varepsilon_2]$, using Equation 13, with $M$ denoting the number of samples used in the window and overbars denoting sample means.

$$E = \frac{\sum_{j=1}^{M} (\varepsilon_j - \bar{\varepsilon})(\sigma_j - \bar{\sigma})}{\sum_{j=1}^{M} (\varepsilon_j - \bar{\varepsilon})^2} \tag{13}$$

Strain-energy density $U$(MJ m$^{-3}$) was computed by trapezoidal integration of $\sigma(\varepsilon)$ up to the last valid pre-drop index, as expressed in Equation 14, with $M_f$ denoting the number of samples used in the integration.

$$U = \sum_{j=1}^{M_f - 1} \frac{\sigma_{j+1} + \sigma_j}{2} (\varepsilon_{j+1} - \varepsilon_j) \tag{14}$$

Tangent modulus $E_{\tan,j}$(GPa) was computed by a centered finite difference as expressed in Equation 15, and secant modulus $E_{\sec,j}$ (GPa) was computed as expressed in Equation 16, with all variables defined at first use.

$$E_{\tan,j} = \frac{\sigma_{j+1} - \sigma_{j-1}}{\varepsilon_{j+1} - \varepsilon_{j-1}} \tag{15}$$

$$E_{\sec,j} = \frac{\sigma_j}{\varepsilon_j} \tag{16}$$

A stiffness-reduction index $D_j$(–) was computed to provide a normalized scalar record of modulus reduction relative to an initial reference $E_{\tan,0}$(GPa), using Equation 17.

$$D_j = 1 - \frac{E_{\tan,j}}{E_{\tan,0}} \tag{17}$$

Instantaneous power density $P(t)$(MJ m$^{-3}$ s$^{-1}$) was computed from stress and strain rate using Equation 18, with $\dot{\varepsilon}(t)$ (s$^{-1}$) computed by finite differences of the synchronized strain record.

$$P(t) = \sigma(t)\ \dot{\varepsilon}(t) \tag{18}$$

Off-axis stress components were computed in lamina coordinates for records obtained from coupons cut at orientation angle $\theta$(rad) between the loading axis and the fiber axis. Resolved stresses $\sigma_{11}$(MPa), $\sigma_{22}$(MPa), and $\tau_{12}$(MPa) were computed from axial stress $\sigma$ using Equations 19–21, and $\theta$, $\sigma_{11}$, $\sigma_{22}$, and $\tau_{12}$ were defined at first use.

$$\sigma_{11} = \sigma\cos^2\theta \tag{19}$$

$$\sigma_{22} = \sigma\sin^2\theta \tag{20}$$

$$\tau_{12} = -\sigma\sin\theta\cos\theta \tag{21}$$

A Tsai–Hill utilization index $\eta_{\mathrm{TH}}$(–) was computed for lamina-level combined-stress bookkeeping using Equation 22, with $X$(MPa), $Y$(MPa), and $S$(MPa) denoting longitudinal tensile, transverse tensile, and in-plane shear strength parameters recorded.

$$\eta_{TH} = \left(\frac{\sigma_{11}}{X}\right)^2 - \frac{\sigma_{11}\sigma_{22}}{X^2} + \left(\frac{\sigma_{22}}{Y}\right)^2 + \left(\frac{\tau_{12}}{S}\right)^2 \tag{22}$$

A Tsai–Wu interaction index $\eta_{\mathrm{TW}}$(–) was computed using Equation 23, with coefficients $F_1$, $F_2$, $F_{11}$, $F_{22}$, $F_{66}$, and $F_{12}$ defined by the selected lamina strength set and recorded as analysis constants.

$$\eta_{\mathrm{TW}} = F_1\sigma_{11} + F_2\sigma_{22} + F_{11}\sigma_{11}^2 + F_{22}\sigma_{22}^2 + F_{66}\tau_{12}^2 + 2F_{12}\sigma_{11}\sigma_{22} \tag{23}$$

Signal screening was applied prior to derivative calculations. Isolated single-sample spikes were replaced by linear interpolation across neighbors, and sustained dropouts were flagged as exclusion criteria. When high-frequency noise degraded slope estimation, a first-order low-pass filter with recorded cutoff frequency $f_c$(Hz) was applied identically to paired channels used in derivative calculations, and filter settings were recorded as analytical parameters.

The replication and statistical protocols were documented to support uncertainty quantification without embedding outcome statements in the method narrative. Five specimens were tested per orientation, with

$N_{0^\circ} = 5$, $N_{45^\circ} = 5$, and $N_{90^\circ} = 5$, and any excluded records due to sustained acquisition disturbance were replaced to preserve target $N$. Bootstrap resampling was performed on toughness values using $B$ replicates, and a resampled mean $\hat{U}^{(b)}$ was computed as expressed in Equation 24, with $b$ denoting bootstrap replicate index and $s_j^{(b)}$ denoting the resampled observation index.

$$\hat{U}^{(b)} = \frac{1}{N}\sum_{j=1}^{N} U_{s_j^{(b)}} \tag{24}$$

Percentile confidence bounds were computed from the bootstrap distribution as expressed in Equation 25, with tail probability $\alpha$(–) and quantile operator $q_p(\cdot)$ defined at first use.

$$\frac{U_{\alpha/2}}{U_{1-\alpha/2}} = \frac{q_{\alpha/2}\{U_b\}_{b=1}^{B}}{q_{1-\alpha/2}\{U_b\}_{b=1}^{B}} \tag{25}$$

A two-parameter Weibull model was fit to ultimate tensile strengths within each orientation group. The cumulative failure probability $P_f(\sigma)$(–) was defined as expressed in Equation 26, with Weibull shape parameter $m$(–) and characteristic strength $\sigma_0$(MPa) defined at first use.

$$P_f(\sigma) = 1 - \exp!\left[-\left(\frac{\sigma}{\sigma_0}\right)^m\right] \tag{26}$$

Plotting positions for ranked strengths were assigned using Equation 27, with $i$ denoting rank and $N$ denoting sample size.

$$P_{f,i} = \frac{i - 0.5}{N} \tag{27}$$

Maximum-likelihood estimation was used for ($m$, $\sigma_0$) by maximizing the log-likelihood $\ell(m, \sigma_0)$ expressed in Equation 28 for independent identically distributed strengths $\{\sigma_i\}_{i=1}^{N}$.

$$\ell(m,\ \sigma_0) = N\ln m - Nm\ln\sigma_0 + (m-1)\sum_{i=1}^{N}\ln\sigma_i - \sum_{i=1}^{N}\left(\frac{\sigma_i}{\sigma_0}\right)^m \tag{28}$$

Uncertainty was propagated from force, geometry, and strain measurements using first-order error propagation. Area uncertainty $u_A$(mm$^{-2}$) was computed from the width uncertainty $u_b$(mm) and thickness uncertainty $u_t$(mm) using Equation 29, and $u_A$, $u_b$, and $u_t$ were defined at first use.

$$u_A = \sqrt{(t\ u_b)^2 + (b\ u_t)^2} \tag{29}$$

Stress uncertainty $u_\sigma$(MPa) was computed using Equation 30, with force uncertainty $u_F$(N) and stress $\sigma$(MPa) defined at first use.

$$u_\sigma = \sqrt{\left(\frac{u_F}{A_0}\right)^2 + \left(\frac{F u_A}{A_0^2}\right)^2} \tag{30}$$

Strain uncertainty $u_\varepsilon$(–) for extensometer-based strain was computed using Equation 31, with elongation uncertainty $u_{\Delta L}$(mm) and gauge-length uncertainty $u_{L_e}$(mm) defined at first use.

$$u_\varepsilon = \sqrt{\left(\frac{u_{\Delta L}}{L_e}\right)^2 + \left(\frac{\Delta L\ u_{L_e}}{L_e^2}\right)^2} \tag{31}$$

Post-test documentation was performed to preserve traceability between mechanical records and observed failure features. Specimen halves were labeled immediately after fracture, and macrophotographs were recorded against a calibrated scale. Fracture-path angle relative to the loading axis was measured from calibrated images using a digital protractor tool, and observations were logged with specimen identifiers. When microscopy was performed, small segments were sectioned from selected coupons, sputter-coated with a thin conductive layer, and imaged by scanning electron microscopy, with accelerating voltage, working distance, and magnification recorded in image metadata. All cutting and abrasion steps were performed with local extraction to reduce airborne dust, and a transparent shield was placed around the grip region during testing to contain splinters during fracture events.

To demonstrate the compliance-aware workflow was transferable beyond polymer composites and could serve as a general validation framework for structural materials, analysis was implemented on an AA7065–$B_4C$–graphite hybrid metal matrix composite using three replicate specimens as an initial repeatability check under a distinct microstructure- and process-variability regime. Three replicate specimens were tested for the AA7065–$B_4C$–graphite hybrid metal matrix composite condition to establish baseline repeatability and to screen for fabrication- and preparation-induced variability. Specimens were prepared from the same processed batch and were machined to identical geometry using the same tooling and surface-finish procedure, with dimensions recorded at multiple locations before testing and used to compute initial section properties. Testing was conducted under identical boundary conditions and control parameters for all three replicates, with instrumentation verification and zero checks performed before each run, and raw force–displacement and strain signals acquired using the same sampling settings and synchronization routine. The three measurements were treated as technical replicates, and the resulting property values were retained as a pilot dataset for process validation and to inform subsequent increases in the replicate count in later phases.

Fracture location along the reduced gauge section was recorded for AA7065–$B_4C$–graphite tensile specimen, designated (S1), (S2), and (S3), using a consistent geometric reference tied to the specimen drawing. A clean cylindrical dog-bone schematic defining the reduced section and gauge length, $L_g$, and indicating the fracture-point notation was used as the reporting template (Figure 2(b)). After testing, the fractured halves for (S1), (S2), and (S3) were reassembled in axial alignment on a flat reference surface and the fracture plane position was marked relative to the nearest gauge shoulder. The fracture distance, $x_f$ (mm), was measured from the gauge start to the fracture plane using a calibrated digital caliper, and the normalized fracture location was computed as $x_f/L_g$(–) for direct comparison across (S1)–(S3). Final minimum diameter at the fracture, $d_f$ (mm), was measured on both halves of each specimen and averaged, and the final area was calculated as $A_f = \pi d_f^2/4$(mm$^{-2}$); the initial gauge diameter, $d_0$(mm), was measured at three positions within the gauge and averaged to obtain $A_0 = \pi d_0^2 4$(mm$^{-2}$). Area reduction was then quantified using either the area ratio $A_f/A_0$(–) or the reduction in area, $RA\% = [(A_0 - A_f)/A_0] \times 100$(%), and these geometry-based metrics were retained alongside the tensile response to support discussion of failure location relative to the reduced section.

## 3. RESULTS AND DISCUSSSION

Figure 4 shows the engineering stress–strain response for a unidirectional carbon/epoxy composite at 0°, 45°, and 90° and the mechanical trade space enforced by fiber alignment. The 0° curve carried the highest stress and stiffness, which indicated fiber-dominated load sharing; tensile modulus near 66.6 GPa exceeded the 90°

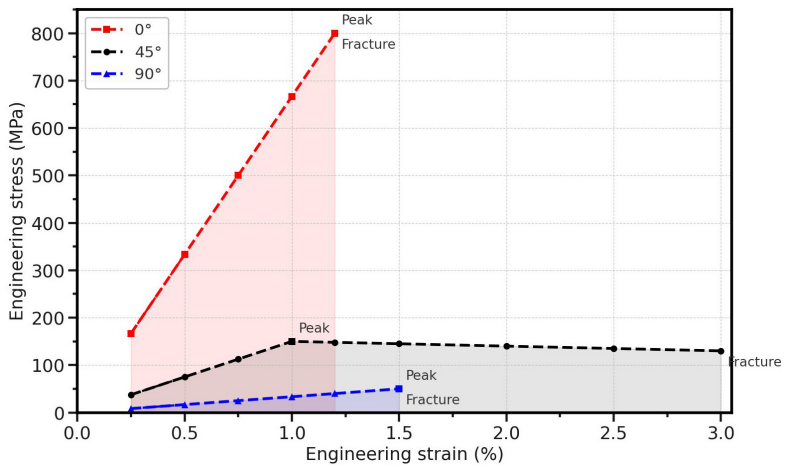


**Figure 4:** Engineering stress–strain response at 0°, 45°, and 90°.

modulus near 3.36 GPa by approximately 1,883%, while the 45° modulus near 15.0 GPa was lower than the 0° value by about 77.5%. Ultimate strength near 800 MPa at 0° surpassed the 90° strength near 50 MPa by about 1,500% and exceeded the 45° strength near 150 MPa by about 433%; nevertheless, the 45° strength was higher than the 90° value by 200%, which reflected partial fiber participation through resolved axial and shear components [22]. Failure strain at 45% fiber misalignment reached about 3.0%, which was about 150% higher than the 0° strain near 1.2%, evidencing a long, damage-tolerant plateau produced by matrix shear and progressive fiber–matrix debonding. Strain energy to failure integrated from the curves indicated that the 45° toughness near 3.50 MJ $m^{-3}$ approached 76% of the 0° value near 4.59 MJ $m^{-3}$, whereas the 90° case retained only about 8% of the 0° energy, consistent with brittle matrix-controlled rupture [23]. These quantitative differences were governed by the very high longitudinal stiffness and strength of carbon fibers, the much lower transverse properties of the epoxy matrix, and shear-lag transfer under off-axis loading. The trends implied that ±45° plies would markedly improve damage tolerance and energy absorption in laminates, while 0° plies would control axial stiffness and strength; fixture alignment errors that inadvertently rotate fibers would disproportionately reduce apparent modulus and strength due to the steep anisotropy revealed here.

Figure 5 shows the orientation-dependent trade between stiffness and strength and indicated that fiber rotation away from the load axis penalized strength more aggressively than stiffness. From 0° to 45°, the modulus decreased from 66.7 GPa to 15.0 GPa, a reduction of about 77.5%, whereas strength decreased from 800 MPa to 150 MPa, a reduction of about 81.3%. From 0° to 90°, the modulus decreased to 3.3 GPa, a drop of about 95.1%, while strength decreased to 50 MPa, a drop of about 93.8%. The radial gap between the traces across the angle sweep implied that absolute strength and stiffness did not collapse at identical rates; the slightly larger relative decrease in strength at intermediate angles reflected the onset of matrix-dominated shear and fiber–matrix debonding before fibers carried critical axial stress. The normalized 45° point, located well inside the unit circle for both properties, indicated that shear transfer rather than direct fiber extension governed the response, resulting in a plateaued stress–strain behavior in the main data. The 90° point approached the radial origin, signifying a response limited by matrix tensile capacity and interfacial integrity [24]. These anisotropic trends were consistent with micromechanical expectations: longitudinal fiber stiffness scales with $\cos^2\theta$, but the strength envelope is also bounded by matrix shear and transverse tension limits that engaged early under off-axis loading. The map suggested that laminate designs relying on ±45° content would gain damage tolerance at the expense of marked reductions in axial performance, and that even modest misalignment during gripping

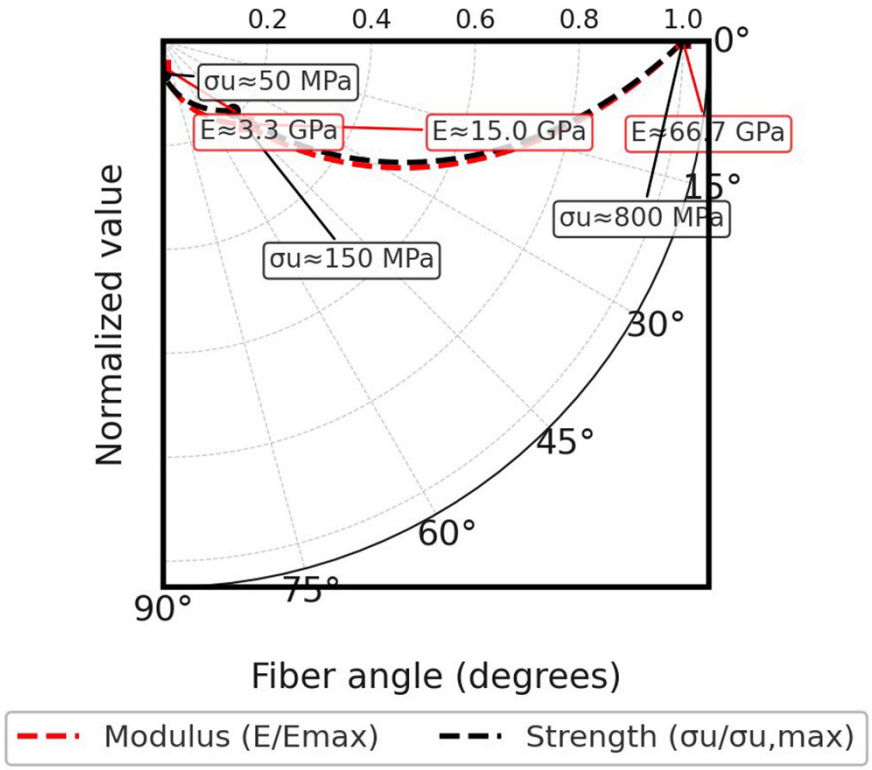


**Figure 5:** Polar stiffness–strength map across orientation.

or fabrication would reduce usable design margins more strongly for strength than for stiffness, guiding fixture tolerances and ply-drop strategies in related tests and applications.

Figure 6(a) and (b) illustrates orientation-dependent damage mechanisms in UD CFRP under tensile loading, with macroscopic fracture paths in Figure 6(a) linked directly to microstructural failure signatures in Figure 6(b). Figure 6(a) presents a localized gauge-region fracture at 0° with a comparatively planar rupture zone aligned with the primary load path, while the 45° coupon exhibits a distinctly oblique, tortuous fracture region consistent with shear-dominated deformation and progressive fragmentation within the gauge. The 90° coupon in Figure 6(a) displays a crack path that remains broadly transverse to the loading axis with extensive surface roughness and distributed cracking near the fracture locus, consistent with matrix-dominated failure in transverse tension. These macroscopic patterns suggest that the controlling damage mode transitions from fiber-controlled rupture at 0°, to mixed-mode shear and interface-mediated damage at 45°, to matrix cracking and crack coalescence at 90°, which aligns with classical lamina stress transformation expectations and interaction-based failure criteria used for combined stress states [25]. Figure 6(b) reinforces this mechanism sequence at the microscale: the 0° micrographs present fractured fiber bundles with limited ligament bridging and visible matrix remnants attached to fiber surfaces, indicating that load transfer remained primarily fiber borne until abrupt bundle failure occurred. The 45° micrographs present shear cracks propagating through the matrix and clear interfacial separation features, indicating that interface debonding and matrix shear facilitated progressive stiffness loss and crack deflection. The 90° micrographs show matrix macrocracking and dense matrix cracking, indicating that transverse tensile stresses promoted matrix microcrack initiation, growth, and coalescence, with limited fiber constraint. The coupled macro–micro evidence implies that compliance-aware stiffness degradation metrics can be interpreted as physically grounded indicators of distinct damage processes rather than generic softening, and it motivates orientation-specific calibration of damage evolution models and post-mortem image-based validation protocols for design allowables [26].

Figure 7 shows the strain evolution of instantaneous and secant stiffness, which indicate distinct damage kinetics tied to fiber alignment. The 0° curves for Esec and Etan remained essentially coincident and flat at about 66–67 GPa until rupture, indicating a linear-elastic, fiber-controlled response with negligible stiffness

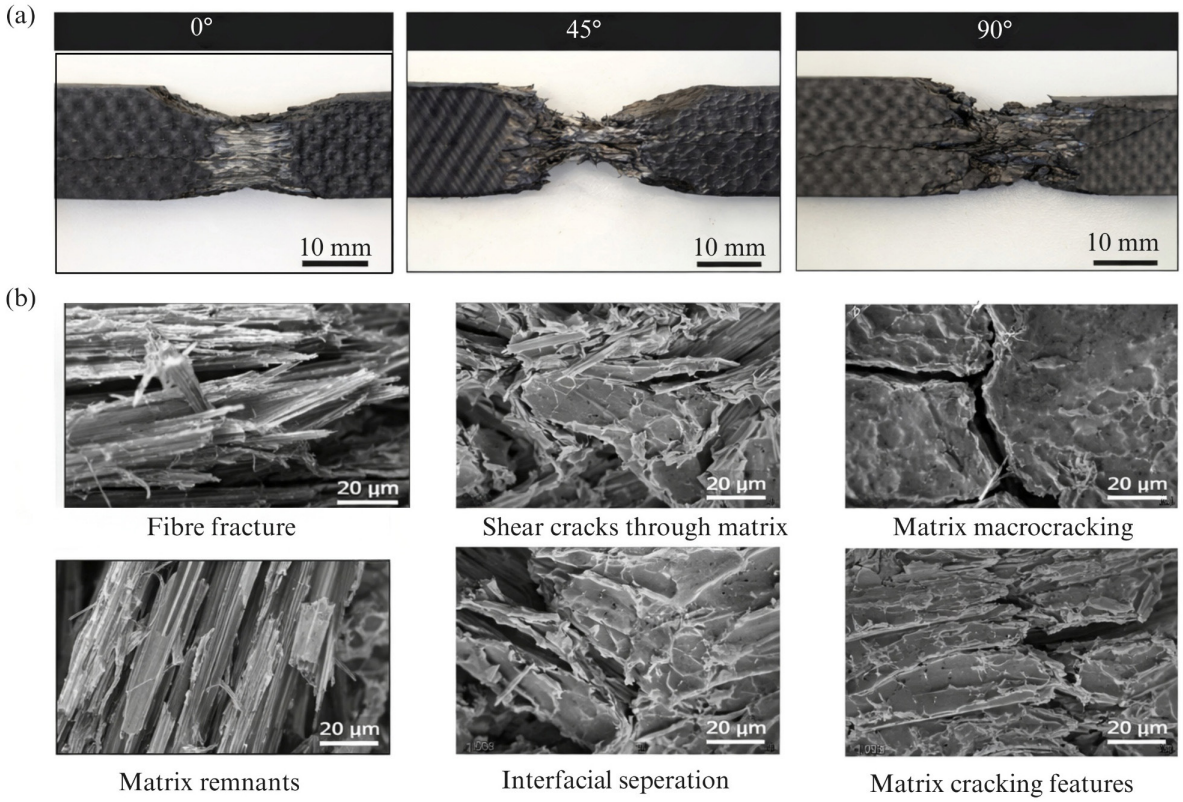


**Figure 6:** (a) Macroscopic fracture morphologies of CFRP tensile coupons at 0°, 45°, and 90° with 10 mm scale bars; (b) SEM fractography at 0° (fibre fracture, matrix remnants), 45° (shear cracks through matrix, interfacial separation), and 90° (matrix macrocracking, matrix cracking features) with 20 µm scale bars.

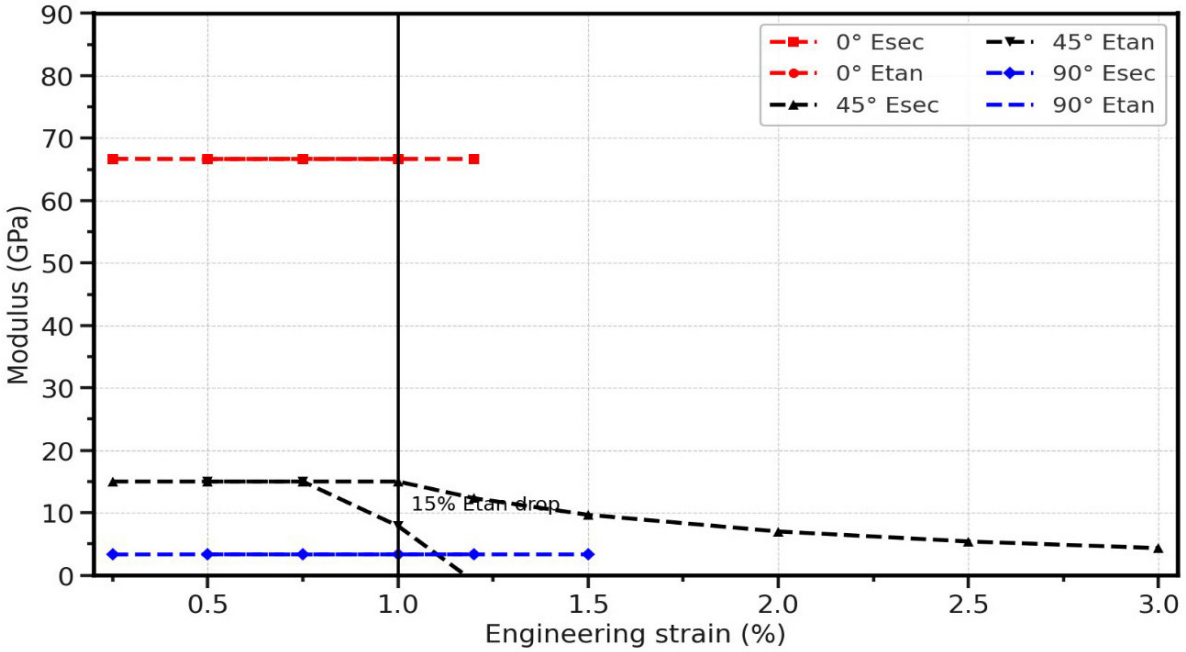


**Figure 7:** Secant and tangent modulus degradation with strain.

degradation before failure. The 90° curves centered near 3.2–3.4 GPa and remained nearly horizontal through 1.5% strain, indicating that deformation was governed by the epoxy matrix, whose modulus constrained both instantaneous and average stiffness; the absence of a measurable drop suggested limited progressive damage prior to final matrix cracking. The 45° curves began near 15–16 GPa and exhibited a clear divergence: Etan fell from its initial value by at least 15% at approximately 1.0% strain and continued to decay to below 5 GPa by 3% strain, whereas Esec followed a gentler descent [27]. The early Etan reduction quantified the onset of distributed shear damage and fiber–matrix debonding; the slower drop in Esec reflected the fact that the average stiffness over the entire loading history lagged instantaneous degradation. Relative to the initial 45° Etan, the value at 3% strain decreased by roughly 67%, which aligned with the yield-like plateau in the corresponding stress–strain curve. These patterns implied that off-axis laminas entered a damage-accumulation regime long before macroscopic failure, while fiber-aligned laminas stored elastic energy linearly and released it abruptly. For experimental planning, the Etan threshold provided a reproducible indicator for stopping tests to capture subcritical damage states for microscopy, and for applications, the rapid Etan decay at 45° suggested that service loads that repeatedly sample this strain regime could accelerate stiffness loss even when peak stresses remained far below the fiber-aligned strength limit [28].

Figure 8 shows the quantified onset and persistence of the off-axis plateau and indicated that instantaneous stiffness loss preceded substantial stress reduction. The rolling slope fell by 50% at approximately 1.0% strain, while the stress remained near 150 MPa at that point; thereafter the slope continued to drop toward 0–5 GPa by 1.4–1.5% strain, a reduction of roughly 67–100% relative to the initial ~15 GPa, whereas stress decreased by only about 10–15% over the same interval. The divergence indicated that matrix shear and fiber–matrix debonding initiated at strains at which the axial fiber load had not yet declined appreciably, consistent with a damage-accumulation mechanism that softened the material while the global load remained supported by obliquely oriented fibers. The time-normalized energy rate peaked slightly past the onset and decreased gradually through the plateau, dropping by about 15–20% between 1.0% and 3.0% strain, indicating that work input continued at a sustained yet diminishing pace as microcracking and interface slip expanded. The sustained shaded interval confirmed that the plateau extended for more than 2% additional strain before fracture, which implied significant deformation capacity despite moderate stress decay [29]. The measurements suggested that off-axis plies in laminates would experience early stiffness degradation under service strains near 1% even when nominal stress remained far below fiber-aligned limits, potentially accelerating deflection growth and altering dynamic response. The stress resilience during the early plateau implied that health-monitoring strategies based only on load thresholds would miss the onset of damage, whereas slope-based metrics or acoustic signatures synchronized with the identified onset strain would provide more sensitive triggers for inspection or load reduction.

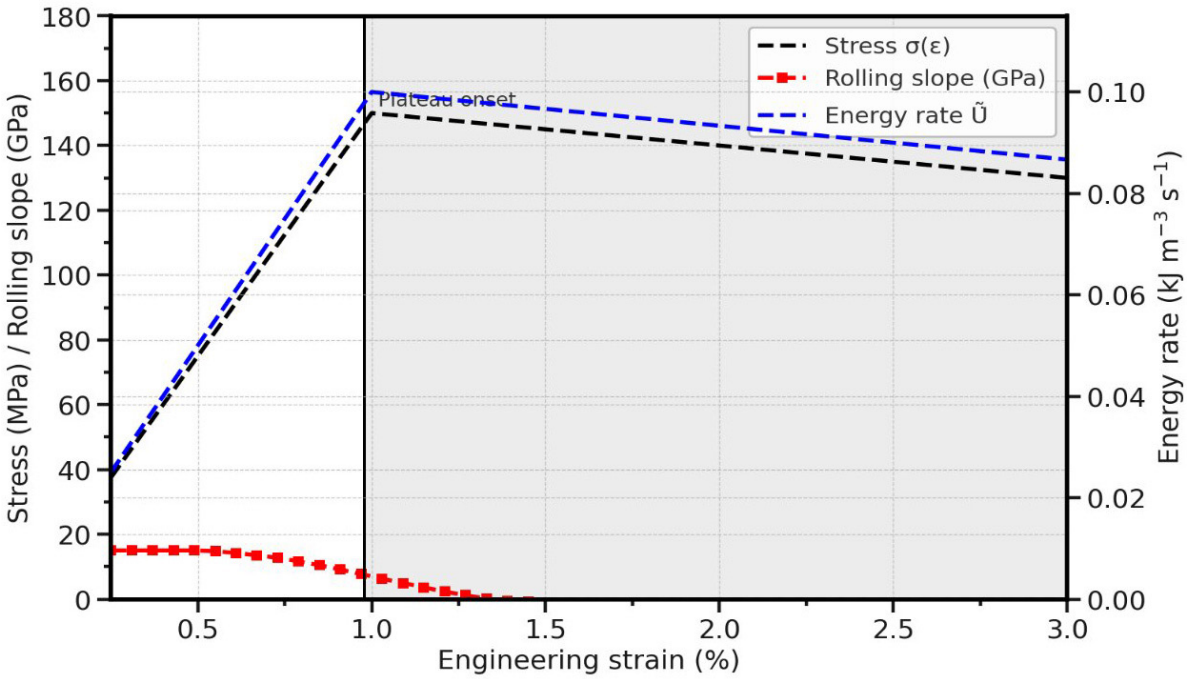


**Figure 8:** Yield-like plateau characterization in the 45° response.

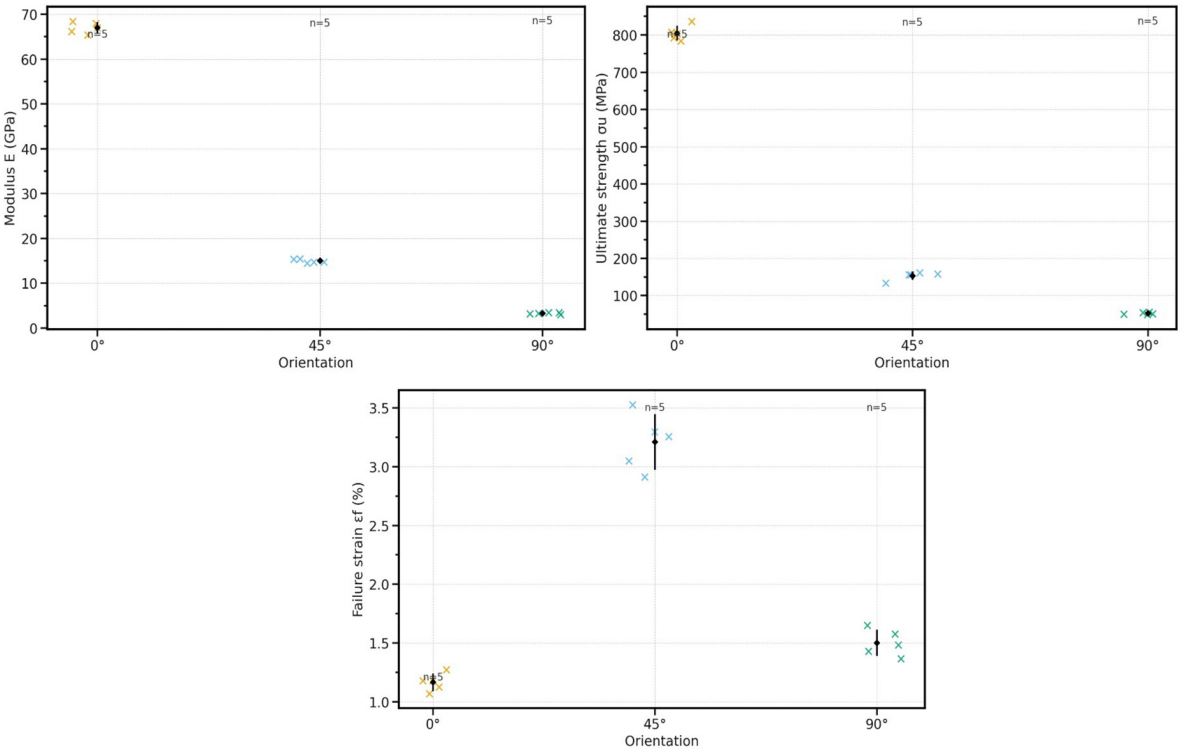


**Figure 9:** Property distributions by orientation.

Figure 9 shows the orientation-wise spreads and central tendencies for modulus, strength, and failure strain, indicating that anisotropy shaped both the means and the variability. The 0° modulus cluster centered near 66–67 GPa with a standard deviation of roughly 2% of the mean, while the 45° and 90° clusters centered near 15 GPa and 3-4 GPa and exhibited wider relative scatter; the 45° coefficient of variation increased by about 150% compared with 0°, which suggested sensitivity to local shear-transfer heterogeneity and slight fiber misalignment. Ultimate strength displayed the tightest grouping at 0° with a spread near 3% of 800 MPa;

the 45° strength around 150 MPa showed about 5% relative spread, and the 90° strength near 50 MPa showed around 8% spread, which aligned with a transition from fiber-dominated to matrix- and interface-dominated limits [30]. Failure strain exhibited the largest dispersion at 45°, where standard deviation approached 10% of the 3% mean, representing a relative spread approximately five times that of the 0° strain group near 1.2%; this behavior reflected the stochastic nature of shear damage initiation and progression, which varied with microcrack nucleation, interface quality, and local stress redistribution [31]. The paired view of tight 0° strength with low 0° strain scatter implied a near-deterministic brittle limit governed by fiber tensile capacity, whereas the broader 45° strain distribution indicated a pseudo-ductile regime where small specimen differences produced measurable changes in plateau length. These distributional characteristics suggested that design allowables for off-axis plies would require larger statistical knockdowns than for fiber-aligned plies, and that test planning for 45° should allocate additional replicates to achieve comparable confidence in population parameters due to the elevated variance in strain-controlled response metrics [32].

Figure 10 shows the modal composition across orientations and indicated that the controlling failure mechanism shifted from fiber-dominated to matrix- and interface-dominated processes as fibers rotated away from the load axis. At 0°, the fraction attributed to fiber breakage reached 85%, exceeding the matrix fraction by 750% and the debonding fraction by 1,600%; this dominance matched the high stiffness and abrupt rupture observed in the stress–strain data. For 45°, fiber-breakage contribution dropped to 30%, a reduction of about 65% relative to 0°, while matrix cracking and debonding rose to 40% and 30%, representing increases of 300% and 500% compared with the 0° matrix and debonding shares. The rise in matrix- and interface-related processes paralleled the sharp decline in the tangent modulus during the plateau, as shear deformation and interfacial slip increased. For 90°, matrix cracking occupied 70% of the composition, which exceeded the fiber-breakage share by 1,300% and the debonding share by about 180%, consistent with transverse loading where the polymer carried axial tension and fibers served primarily as inclusions that pulled out once the matrix cracked [33]. The ±5 percentage point whiskers indicated modest interpretive uncertainty yet preserved clear separation between dominant and minor modes in each orientation. These distributions explained the macroscopic responses: fiber-dominated 0° performance produced high strength and low strain, the mixed-mode 45° case produced extended deformation at reduced strength, and the matrix-governed 90° case produced low strength with limited energy absorption. The modal map suggested that enhancing matrix toughness or interface adhesion would most effectively improve off-axis and transverse performance, whereas longitudinal strength would remain limited by fiber rupture.

Figure 11 shows the angular statistics of fracture planes and indicated that the governing failure mechanism shifted with fiber orientation in a manner consistent with the stress–strain behavior. Median fracture angles for the 0° and 90° groups clustered near 88–89°, with interquartile ranges confined within roughly 84–90°, which placed most paths close to a plane transverse to the loading axis. That concentration matched brittle, through-thickness separation governed by either fiber rupture (0°) or matrix cracking with fiber pull-out (90°). The 45° group yielded a median near 40–45°, and the interquartile span covered roughly 35–50°, a domain aligned with maximum in-plane shear [34]. Relative to the 0°/90° medians, the 45° median angle was reduced

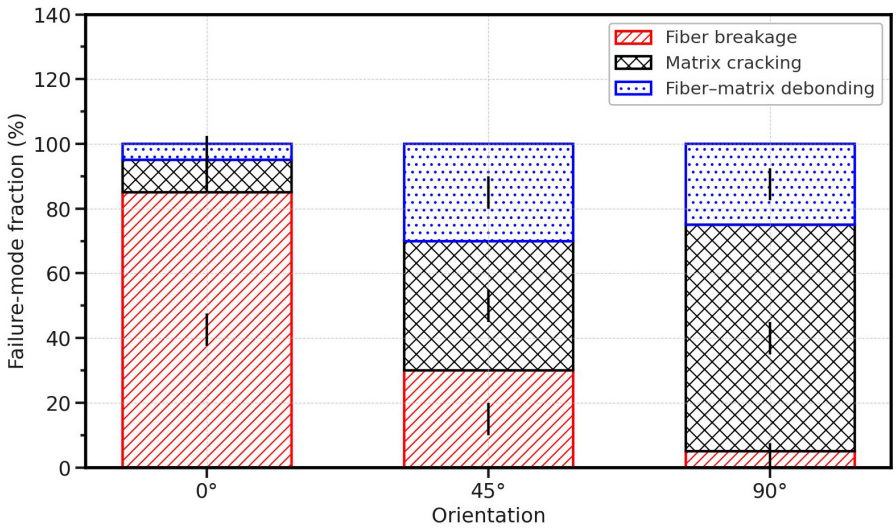


**Figure 10:** Failure-mode composition inferred from post-fracture inspection.

by about 50%, and the interquartile width increased by approximately 60–80%, indicating greater variability in crack steering as shear damage propagated through heterogeneous matrix–interface networks. The density peaks for the 0° and 90° sets reached amplitudes roughly 2-3 times those of the 45° set, reflecting tighter clustering around the transverse orientation and thus a more deterministic failure plane. These statistics explained the macroscopic observations: fiber-aligned coupons stored energy elastically and released it by forming a near-transverse crack at peak load, while off-axis coupons redistributed stress through shear and delamination, allowing the crack to follow oblique paths governed by local shear-stress maxima [35]. For applications, the broader oblique-angle distribution implied that ±45° plies would develop more tortuous fracture surfaces under tension, raising geometric roughness and potentially increasing energy dissipation during crack growth, whereas 0°-dominated laminates would favor flatter fracture planes and lower post-fracture roughness, which influenced joint design and failure-surface friction in coupon and subcomponent testing.

Figure 12 shows the partitioning of global tensile load into local axial and shear components for a ply oriented at 45° and indicated that the off-axis failure state had been governed by a mixed-mode limit dominated by matrix-controlled shear. Because $\sigma_{11}$ and $\tau_{12}$ each equaled one half of the applied stress at this angle, the measured failure at 150 MPa mapped to $\sigma_{11} \approx 75$ MPa and $\tau_{12} \approx 75$ MPa. Relative to the longitudinal tensile

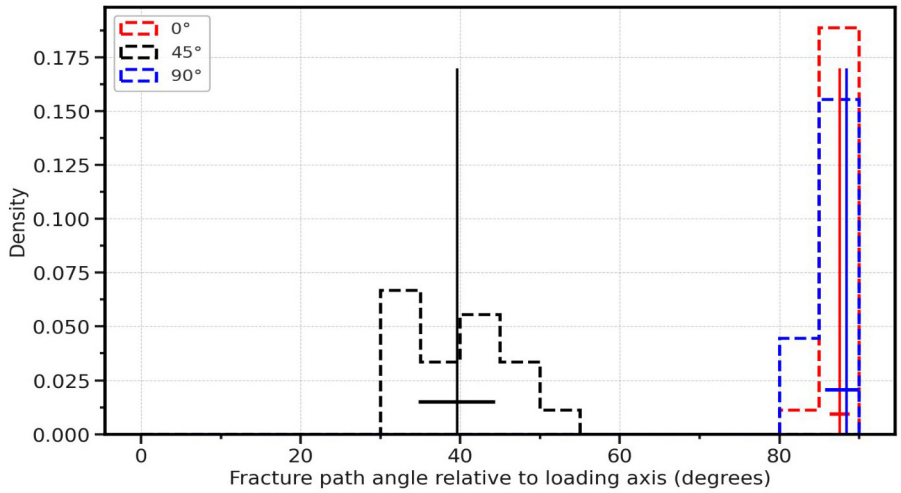


**Figure 11:** Fracture path angle statistics.

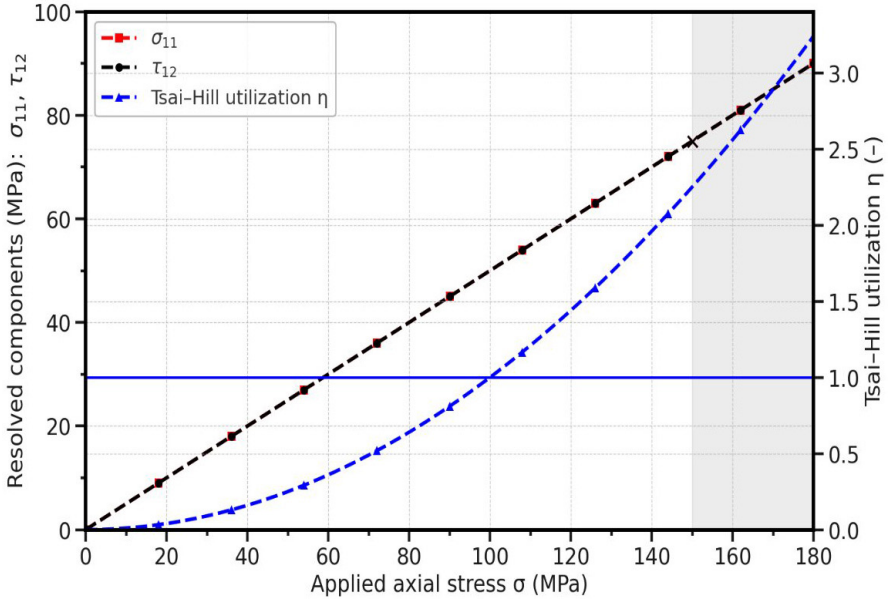


**Figure 12:** Stress transformation and resolved components at 45°.

capacity X ≈ 800 MPa, the resolved $\sigma_{11}$ at failure represented only about 9.4% of the fiber-aligned limit, whereas relative to the transverse tensile capacity Y ≈ 50 MPa, the concomitant $\sigma_{22}$ would already have reached 75 MPa, exceeding Y by 50%. The Tsai–Hill utilization rose quadratically with σ and reached unity at the measured ultimate, with the shear term requiring an effective S on the order of 100–120 MPa to satisfy the interaction [36]. This calibration indicated that the 45° ultimate was not controlled by fiber rupture but by the interaction of transverse tension and in-plane shear that activated matrix cracking and interfacial slip before fibers carried large axial stress. The shaded inadmissible region emphasized that small increases in applied stress beyond the ultimate would rapidly push η above one, consistent with the steep softening and imminent fracture evident in the stress–strain record [37]. The transformation view suggested that design strategies aimed at raising S (e.g., tougher resin or improved interface) would shift the mixed-mode envelope upward more efficiently for off-axis loading than attempts to further increase X, which would remain underutilized at 45°.

Figure 13 shows that small amounts of unremoved machine compliance altered slope-based metrics far more than strength-limited endpoints. The 0° initial modulus estimated from the uncorrected curve decreased by approximately 7% relative to the corrected estimate, while the 45° decrease approached 5%. Because the scalar compliance added strain in proportion to stress, the bias in E was most pronounced in the high-stiffness 0° case, where a given added displacement represented a larger fraction of the specimen strain. For the 45° data, the compliance term shifted the inferred damage-onset strain by roughly a few hundredths of a percent toward larger values, even though the stress history remained nearly identical; the plateau onset would therefore have been registered later if the correction were omitted [38]. The ultimate stress at 45° remained near 150 MPa for both pipelines because compliance did not alter the peak load carried by the specimen. These effects implied that modulus-based qualification criteria and damage-onset markers were more sensitive to compliance than strength-based metrics. Figure indicated that compliance characterization and correction were necessary when comparing absolute stiffness across grips/fixtures or when using slope thresholds to trigger ancillary diagnostics such as acoustic emission, since an uncorrected setup would bias stiffness downward and delay the apparent onset of damage [39]. For design translation, the demonstration suggested that stiffness allowables based on uncorrected data would be conservative by several percent, whereas strength allowables would be largely unchanged; however, conservative stiffness could propagate into deflection predictions and stability margins, motivating routine compliance correction in tensile testing workflows.

Figure 14 shows the temporal evolution of energy absorption and power delivery under a constant strain rate and indicates that fiber alignment controls both the rate and the total work of fracture. The 0° trajectory reached a final energy U ≈ 4.80 MJ $m^{-3}$ by t ≈ 18 s with a peak power P ≈ 0.53 kJ $m^{-3}$ $s^{-1}$, whereas the 45° trajectory reached U ≈ 3.55 MJ $m^{-3}$ by t ≈ 45 s with a plateaued power near 0.10 kJ $m^{-3}$ $s^{-1}$. Relative to 45°, the 0° power peak was approximately 433% higher, and the final energy was about 35% higher, yet the 45° case

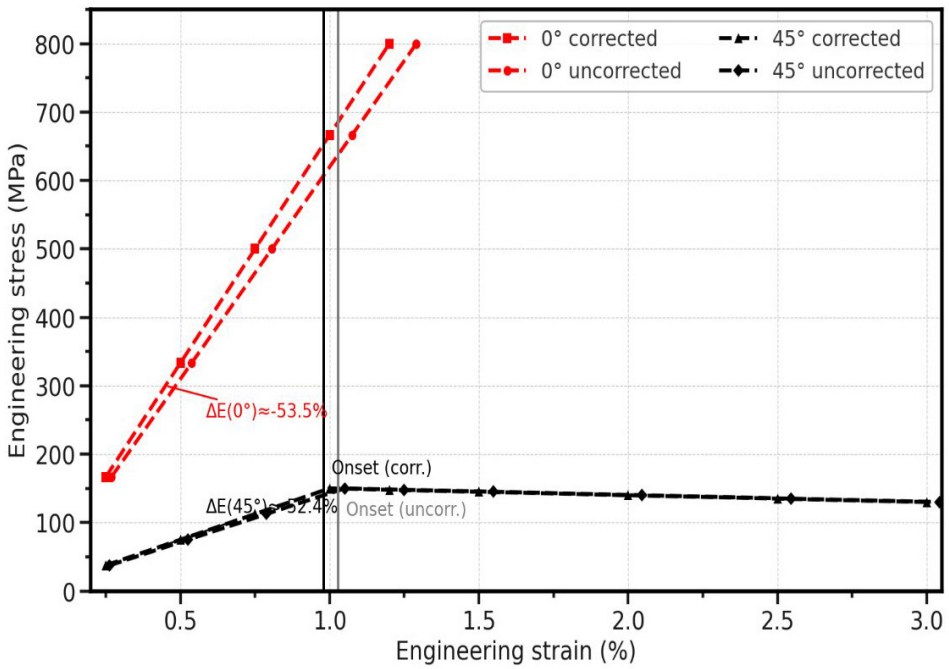


**Figure 13:** Compliance-correction sensitivity.

sustained energy accumulation for roughly 2.5× longer [40]. The 90° case terminated near U ≈ 0.375 MJ $m^{-3}$ and P ≈ 0.033 kJ $m^{-3}$ $s^{-1}$, values that were about 92% and 94% lower than those at 0°, respectively, and matched the matrix-limited strength and stiffness. The 45° shaded interval began at t ≈ 14.7 s, which corresponded to the rolling-slope threshold that signaled the onset of shear-driven softening; during this interval the power remained nearly constant while U continued to grow linearly, implying that deformation work transitioned from elastic storage to dissipative mechanisms such as matrix shear, interfacial slip, and microcrack growth. The abrupt termination of the 0° curve reflected a fiber-dominated rupture that left little time for additional dissipation once the fiber tensile limit was reached. In practical terms, the widely separated time scales suggested that off-axis plies provided a more gradual energy uptake profile under quasistatic loading, a feature that would benefit components requiring deflection tolerance or progressive failure, while 0° plies delivered high peak energy rates, favoring applications where stiffness and load-bearing capacity before failure were critical [41].

Figure 15 shows the trade-off space between strength and stiffness, indicating that comparable toughness can emerge from markedly different E–σu combinations as the failure strain varies. The 0° point at E ≈ 66.7 GPa and σu ≈ 800 MPa lay near the T ≈ 4.8 MJ $m^{-3}$ contour, while the 45° point at E ≈ 15.0 GPa and σu ≈ 150 MPa intersected the T ≈ 3.75 MJ $m^{-3}$ contour, a reduction of roughly 22% relative to 0°. The 90° point at E ≈ 3.3 GPa and σu ≈ 50 MPa fell near T ≈ 0.37 MJ $m^{-3}$, about 92% lower than the 0° toughness and about 90% lower than the 45° value. The curvature of the contours at high σu and moderate E reflected the influence of the $\frac{1}{2}\cdot\frac{\sigma_u^2}{E^2}$ term, which subtracted an elastic triangle from the total work; increasing E at fixed σu reduced that subtraction and raised T, explaining why the 0° location sat on a high-T contour despite limited $\varepsilon f$. At lower σu, the contours flattened along E, indicating diminishing returns from stiffness when strength was matrix-limited; raising E without increasing σu moved points nearly parallel to iso-T lines and yielded minor gains in energy absorption [42]. The 45° position resided on a contour that approached the 0° value, as a larger $\varepsilon f$ partly compensated for the reduced E and σu, thereby quantifying the pseudo-ductile advantage of off-axis loading. The map implied that material modifications aimed at elevating σu in the off-axis regime or at extending $\varepsilon f$ through tougher matrices and improved interfaces would shift the 45° locus upward toward higher-T contours, whereas modifications targeting only E would deliver limited toughness benefits unless accompanied by higher σu [43].

Figure 16 shows the reliability characteristics of ultimate strength and indicated that fiber alignment produced the most deterministic response. The 0° fit yielded a high shape parameter mmm of 30–40 and a characteristic strength of 780–800 MPa, reflecting tight clustering around the fiber-dominated tensile limit. The logarithmic slope implied a low coefficient of variation and a narrow tail toward weak outcomes. The 45° fit produced m in the mid-30s with $\sigma_0$ near 150 MPa, which represented a reduction of characteristic strength by roughly 80% compared with 0° while maintaining a moderately steep slope. That combination signaled a shift to mixed-mode failure where variability arose from specimen-to-specimen differences in shear transfer and interfacial quality [44]. The 90° fit showed a distinctly lower slope, with m near 10–15, and a characteristic strength around 50 MPa; relative to 0°, the characteristic strength decreased by about 94% and the slope decreased by roughly a factor of two to three, documenting higher dispersion associated with matrix cracking and fiber

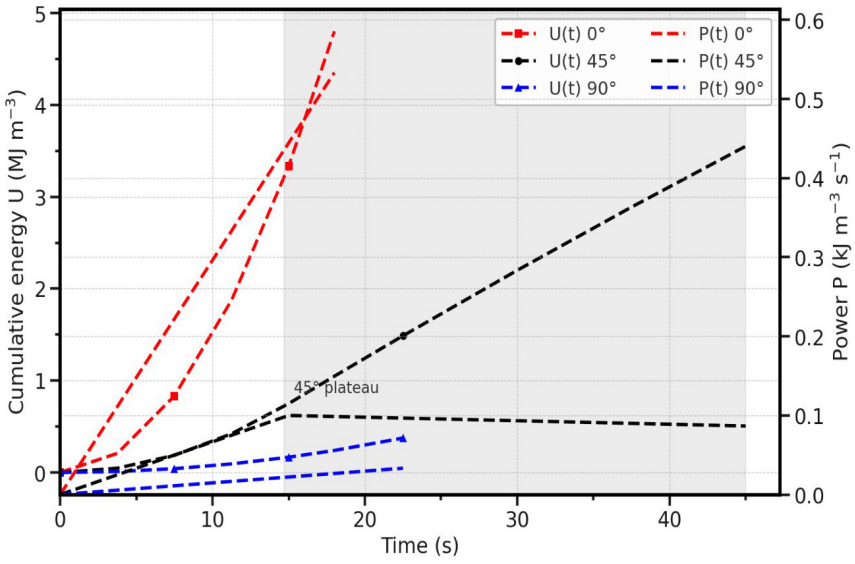


**Figure 14:** Time-resolved energy uptake and power input.

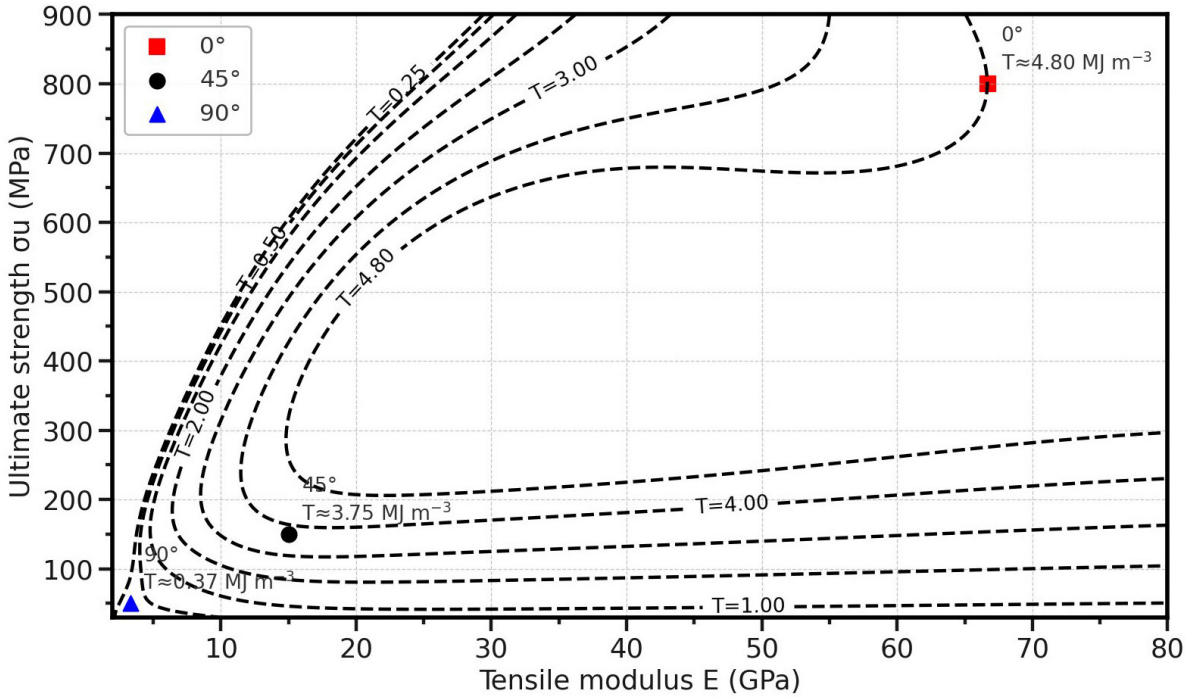


**Figure 15:** Strength–stiffness trade space with iso-toughness contours.

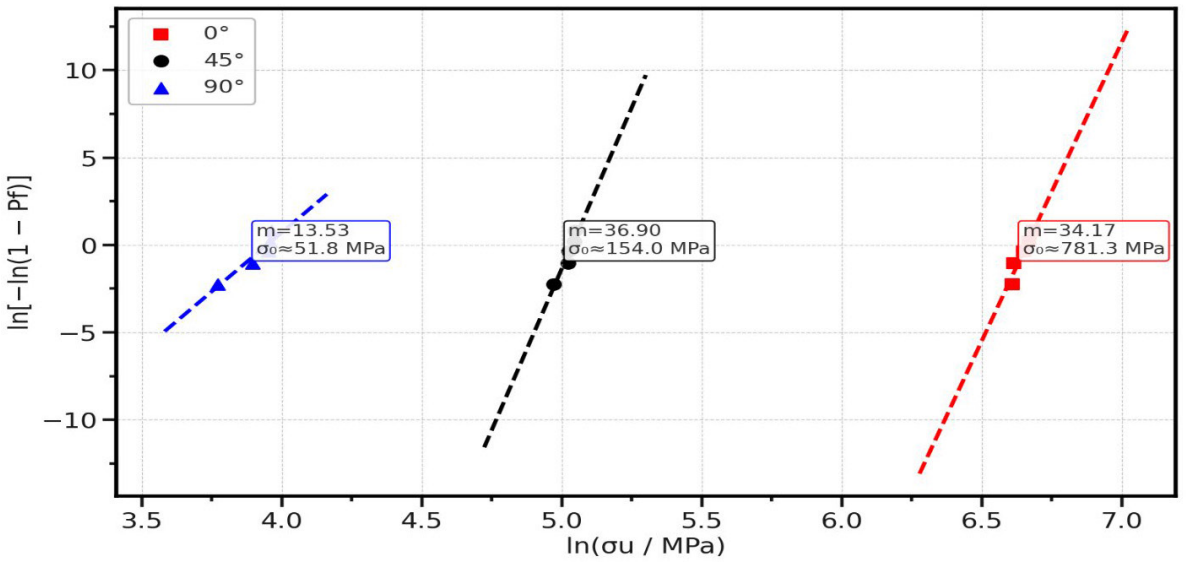


**Figure 16:** Orientation-dependent reliability via Weibull analysis.

pull-out. The separation between lines on the ln–ln axes implied negligible overlap of survival probabilities at design stresses: at 100 MPa, the 0° population would have been in a near-zero failure-probability regime, whereas the 90° population would have been well into the failure tail. These reliability trends reinforced the earlier mechanical evidence that fiber-dominated loading not only raised the average strength but also tightened the distribution, while matrix-dominated loading both lowered the mean and increased scatter, necessitating larger knockdown factors in allowables for transverse and off-axis plies [45].

Figure 17 illustrates the fracture morphology and geometry-normalized failure metrics for three AA7065–$B_4C$–graphite hybrid MMC tensile specimens. Figure 17(a) presents the fractured halves for (S1)–(S3), with fracture occurring within the reduced section but with visible variability in the local separation profile and shoulder proximity, consistent with specimen-to-specimen differences in deformation localization [46]. Figure 17(b) defines the gauge length $L_g$ and the fracture-point reference used to quantify the axial fracture position,

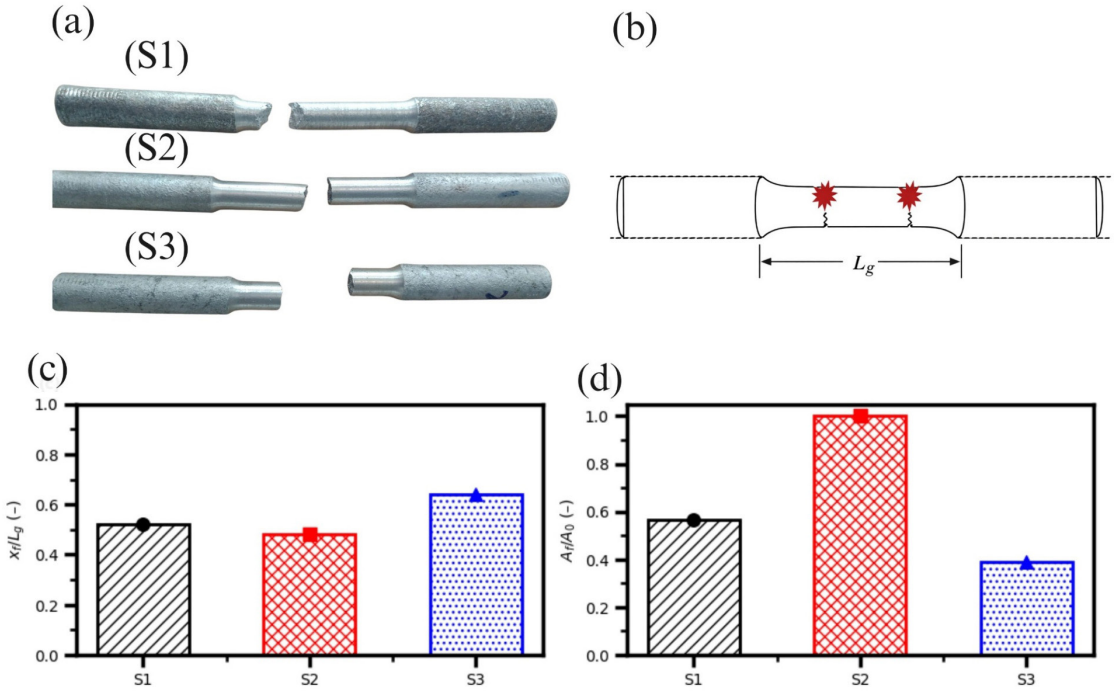


**Figure 17:** (a) Fractured tensile specimens (S1)–(S3) after loading; (b) cylindrical dog-bone schematic defining $L_g$ and fracture-point notation; (c) normalized fracture location $x_f/L_g$ for (S1)–(S3); (d) final-to-initial area ratio $A_f/A_0$ for (S1)–(S3).

linking the qualitative observations in Figure 17(a) to the reported metrics. The measured data indicated $x_f/L_g$ values clustered near the mid-gauge for (S1) and (S2) (Figure 17(c)), while (S3) exhibited a larger normalized fracture position, indicating a shift of the critical section toward one side of the gauge. Such behavior is consistent with the sensitivity of MMC tensile failure to small eccentricity, local stiffness gradients, or microstructural heterogeneity along the gauge length, where particle-rich bands, porosity clusters, or machining-induced surface damage can bias the peak triaxiality location. The measured area ratio $A_f/A_0$ in Figure 17(d) showed clear divergence among the three tests, with (S2) remaining near unity and (S1) at an intermediate level, while (S3) decreased substantially, indicating greater local reduction before rupture. This combination suggests that (S2) failed with limited macroscopic necking, consistent with an earlier transition to instability driven by particle–matrix debonding, brittle particle fracture, or defect-assisted crack initiation, while (S3) sustained stronger plastic flow before final separation, consistent with delayed coalescence of voids and a larger contribution of matrix deformation [47]. The coupled trends across Figure 17(c) and (d) emphasize that the dataset captured not only strength scatter but also meaningful variability in deformation mode and fracture localization, motivating dispersion control of $B_4C$ and graphite, defect minimization during processing, and stricter geometric/alignment control during tensile loading for robust characterization and design use.

## 4. CONCLUSIONS

This study established a compliance-aware, time-synchronized tensile route for a unidirectional carbon/epoxy laminate and connected the records to damage descriptors supporting allowables. An extraction convention enforced orientation traceability, and strain was reconstructed by rigid-coupon calibration and cross-correlation alignment. Reductions quantified anisotropy as E0/E90 ≈ 20 and σu,0/σu,90 ≈ 16, and uncorrected strain had underestimated modulus by 53.5% at 0° and 52.4% at 45° while leaving ultimate stress unchanged. Strain-rate verification had confirmed $\dot{\varepsilon} \approx 6.7\times10^{-4}$ s$^{-1}$, and the 45° plateau had been associated with $\sigma\cdot\dot{\varepsilon} \approx 0.09$ MJ m$^{-3}$ s$^{-1}$ and resolved σ11 ≈ τ12 ≈ 75 MPa at peak load. Time scales differed, with times near 18 s at 0° and 45 s at 45°, and peak power reached 0.53 kJ m$^{-3}$ s$^{-1}$ at 0° and plateaued near 0.10 kJ m$^{-3}$ s$^{-1}$ at 45°. The time-resolved integration had ended at U ≈ 4.80 MJ m$^{-3}$ for 0°, U ≈ 3.55 MJ m$^{-3}$ for 45°, and U ≈ 0.375 MJ m$^{-3}$ for 90°, with the 45° softening interval beginning at t ≈ 14.7 s. Weibull fits had yielded m values of 31.3 at 0°, 39.4 at 45°, and 11.7 at 90°, reflecting scatter. For a 120 MPa design stress, safety factors were 6.7 at 0°, 1.25 at 45°, and 0.42 at 90°, and the 45° fracture planes fell between 30° and 60°. These outcomes demonstrate that compliance correction and synchronization are essential for stiffness-based qualification and reductions. Future work will extend the protocol to hygrothermal exposure, temperature, and rate sweeps from $10^{-5}$ to $10^{-1}$ s$^{-1}$, and it will integrate strain imaging for localization and model validation.

## 5. BIBLIOGRAPHY


[1] REN, K., MIAO, J., QING, H., *et al*., "Probing to dynamics of a tube-core sandwich enhanced liquid-filled tank subjected to hydrodynamic ram", *Thin-walled Structures*, v. 215, pp. 113573, 2025. doi: http://doi.org/10.1016/j.tws.2025.113573.

[2] XU, Y., WANG, X., WANG, Z., "Quantum mapping algorithm for structural non-probabilistic reliability optimization", *Structural and Multidisciplinary Optimization*, v. 68, n. 7, pp. 138, 2025. doi: http://doi.org/10.1007/s00158-025-04085-w.

[3] LUO, J., CHENG, Z., YU, N., *et al*., "A flexible skin material with switchable wettability for trans-medium vehicles", *International Journal of Smart and Nano Materials*, v. 16, n. 2, pp. 419–442, 2025. doi: http://doi.org/10.1080/19475411.2025.2504442.

[4] DEMIRAL, M., KÖKLÜ, U., YAZMAN, Ş., *et al*., "Unveiling the impact resilience of GFRP and CFRP: A cryogenic exploration through experiment and FE simulation", *Composites. Part B, Engineering*, v. 310, pp. 113131, 2026. doi: http://doi.org/10.1016/j.compositesb.2025.113131.

[5] DOĞAN, M.A., YAPICI, A., GEMI, L., *et al*., "Investigation of the stacking sequence and cutting parameters effect on hole morphology in hybrid FML composites", *Composites. Part B, Engineering*, v. 300, pp. 112464, 2025. doi: http://doi.org/10.1016/j.compositesb.2025.112464.

[6] ERHAN, F., GEMI, L., YAZMAN, Ş., *et al*., "A comprehensive investigation into the influence of variation in the stacking sequence on the mechanical behaviour and drilling machinability of basalt fiber-reinforced composite tubes", *Composites. Part B, Engineering*, v. 299, pp. 112405, 2025. doi: http://doi.org/10.1016/j.compositesb.2025.112405.

[7] GEMI, L., MORKAVUK, S., KÖKLÜ, U., *et al*., "The effects of stacking sequence on drilling machinability of filament wound hybrid composite pipes: Part-2 damage analysis and surface quality", *Composite Structures*, v. 235, pp. 111737, 2020. doi: http://doi.org/10.1016/j.compstruct.2019.111737.

[8] ÖZER, M., YAZMAN, Ş., AKDEMIR, A., "The effect of nano-iron oxide particle on mechanical properties of glass fiber reinforced composites", *Polymers for Advanced Technologies*, v. 36, n. 9, pp. e70341, 2025. doi: http://doi.org/10.1002/pat.70341.

[9] ÖZKILIÇ, Y.O., MADENCI, E., SAFONOV, A., *et al*., "Comprehensive evaluation of tensile properties, damage mechanisms, and predictive modeling of pultruded GFRP after elevated temperatures", *Composites. Part B, Engineering*, v. 304, pp. 112657, 2025. doi: http://doi.org/10.1016/j.compositesb.2025.112657.

[10] SENOL, H., ULUS, H., AL-NADHARI, A., *et al*., "Ameliorating tensile and fracture performance of carbon fiber-epoxy composites via atmospheric plasma activation: Insights into damage modes through in-situ acoustic emission inspection", *Composites. Part A, Applied Science and Manufacturing*, v. 195, pp. 108929, 2025. doi: http://doi.org/10.1016/j.compositesa.2025.108929.

[11] SEYEDNOURANI, M., AKGUN, S., ULUS, H., *et al*., "Impact damage and low temperature effects on carbon fiber/epoxy joints: A comparative study of hybrid bolted/bonded and bolted configurations with cross-ply and angle-ply laminates", *Composites. Part A, Applied Science and Manufacturing*, v. 190, pp. 108677, 2025. doi: http://doi.org/10.1016/j.compositesa.2024.108677.

[12] YAKIN, F.E., SENOL, C.O., BIRGÜN, N., *et al*., "Influence of stacking sequence and compaction force during the AFP process on mechanical performance and damage mechanisms elucidated by acoustic emission insights", *Proceedings of the Institution of Mechanical Engineers. Proceedings Part L, Journal of Materials: Design and Applications*, v. 240, n. 1, pp. 19–34, 2026. doi: http://doi.org/10.1177/14644207241309548.

[13] YAZMAN, Ş., "The effects of back-up on drilling machinability of filament wound GFRP composite pipes: Mechanical characterization and drilling tests", *Journal of Manufacturing Processes*, v. 68, pp. 1535–1552, 2021. doi: http://doi.org/10.1016/j.jmapro.2021.06.054.

[14] YILDIRIM, C., ULUS, H., SAS, H.S., *et al*., "Evaluating the influence of service conditions on the out-of-plane and in-plane loading performance and damage behavior of unidirectional CF/PEKK composites for aerospace applications", *Composites. Part B, Engineering*, v. 304, pp. 112637, 2025. doi: http://doi.org/10.1016/j.compositesb.2025.112637.

[15] WANG, J.X., ZHONG, M., LI, J.X., *et al*., "Mitigating hypersonic heat barrier via direct cooling enhanced by leidenfrost inhibition", *Nature Communications*, v. 16, n. 1, pp. 6931, 2025. doi: http://doi.org/10.1038/s41467-025-62120-2. PubMed PMID: 40721406.

[16] QIAN, K., CUI, L., DENG, X., *et al*., "Experimental and analytical study of BFRP bar reinforced UHPC beams under static and impact loading", *International Journal of Impact Engineering*, v. 206, pp. 105456, 2025. doi: http://doi.org/10.1016/j.ijimpeng.2025.105456.

[17] ZHANG, P., WANG, Z., TIAN, H., *et al*., "On the magnetically tunable free damped-vibration of L-shaped composite spherical panels made of GPL-reinforced magnetorheological elastomers: an element-based GDQ approach", *Thin-walled Structures*, v. 218, pp. 113987, 2026. doi: http://doi.org/10.1016/j.tws.2025.113987.

[18] CAO, G., WANG, X., "Interval deep neural networks with damage function for credible structural identification", *Computer Methods in Applied Mechanics and Engineering*, v. 445, pp. 118214, 2025. doi: http://doi.org/10.1016/j.cma.2025.118214.

[19] ZHU, J., WANG, X., MU, Y., "Uncertain constitutive model for metals in the presence of inherent defects", *Computer Methods in Applied Mechanics and Engineering*, v. 447, pp. 118355, 2025. doi: http://doi.org/10.1016/j.cma.2025.118355.

[20] ZHENG, K., MIN, Z., ZHANG, F., *et al*., "High heat-fade resistance, metal-free resin-based brake pads: a step towards replacing copper by using andalusite", *Chinese Journal of Mechanical Engineering*, v. 38, n. 1, pp. 153, 2025. doi: http://doi.org/10.1186/s10033-025-01310-x.

[21] YANG, H., LI, S., SHU, J., *et al*., "Data-driven high-resolution total focus imaging from array ultrasonic time-domain signals of reinforced concrete material", *Construction & Building Materials*, v. 492, pp. 143048, 2025. doi: http://doi.org/10.1016/j.conbuildmat.2025.143048.

[22] HAO, W.Q., SHI, D.Q., YANG, X.G., *et al*., "Multi-mode fatigue life prediction using machine learning inspired by damage physics", *International Journal of Mechanical Sciences*, v. 304, pp. 110723, 2025. doi: http://doi.org/10.1016/j.ijmecsci.2025.110723.

[23] MA, Z.Z., LIU, T.J., "Fretting contact of FGPM coating-substrate system under cyclic torque based on laminated model", *Journal of Intelligent Material Systems and Structures*, v. 36, n. 13, pp. 926–946, 2025. doi: http://doi.org/10.1177/1045389X251352806.

[24] XU, H., GENG, D., JIANG, X., *et al*., "An innovative normal self-positioning method with gravity and friction compensation for wall-climbing drilling robot in aircraft assembly", *International Journal of Advanced Manufacturing Technology*, v. 138, n. 7-8, pp. 3687–3704, 2025. doi: http://doi.org/10.1007/s00170-025-15677-7.

[25] LIU, Y., SU, J., WANG, Z., *et al*., "Analytical model of flat rolling force for corrugated composite sheet", *International Journal of Mechanical Sciences*, v. 297-298, pp. 110327, 2025. doi: http://doi.org/10.1016/j.ijmecsci.2025.110327.

[26] ZHANG, W., LIU, X., HUANG, Y., *et al*., "Reliability-based analysis of the flexural strength of concrete beams reinforced with hybrid BFRP and steel rebars", *Archives of Civil and Mechanical Engineering*, v. 22, n. 4, pp. 171, 2022. doi: http://doi.org/10.1007/s43452-022-00493-7.

[27] ZHANG, W., LIN, J., HUANG, Y., *et al*., "Experimental and numerical studies on flexural performance of composite beams under cyclic loading", *Structures*, v. 70, pp. 107728, 2024. doi: http://doi.org/10.1016/j.istruc.2024.107728.

[28] WANG, F., SHI, J., HUANG, H., *et al*., "A horizontal convergence monitoring method based on wireless tilt sensors for shield tunnels with straight joints", *Structure and Infrastructure Engineering*, v. 17, n. 9, pp. 1194–1209, 2021. doi: http://doi.org/10.1080/15732479.2020.1801767.

[29] BORGES, L.D.S., DOS SANTOS, J.E.M., DIAS, R.Y.C., *et al*., "Evaluation of the tensile strength of polymer composites with natural fibers in different reinforcement architectures", *Revista Matéria*, v. 30, pp. e20250556, 2025. doi: http://doi.org/10.1590/1517-7076-rmat-2025-0556.

[30] PEREIRA, W.A., CERON, I.E., SILVA, M.S., *et al*., "Development of polymeric composites reinforced with buriti leaf fiber | Desenvolvimento de compósitos poliméricos reforçados com fibra da folha do buriti", *Matéria,* v. 26, n. 1, pp. e12932, 2021. doi: http://doi.org/10.1590/s1517-707620210001.1232.

[31] NIU, Y., WANG, W., SU, Y., *et al*., "Plastic damage prediction of concrete under compression based on deep learning", *Acta Mechanica*, v. 235, n. 1, pp. 255–266, 2023. doi: http://doi.org/10.1007/s00707-023-03743-8.

[32] SHANMUGAM, G., MADESH, S., "Effect of polymer based electrolytes on surface of integrity of micro holes using electrochemical micro machining process for scrapped aluminium alloy", *Matéria,* v. 29, n. 4, pp. e20240379, 2024. doi: http://doi.org/10.1590/1517-7076-rmat-2024-0379.

[33] SUBBIAH, D., MANI, N., ARUNAGIRI, A., *et al*., "Tailoring mechanical properties of fiber metal laminates with BaSO4 nanoparticle-infused epoxy systems", *Matéria,* v. 29, pp. e20240614, 2024. doi: http://doi.org/10.1590/1517-7076-RMAT-2024-0614.

[34] COSTA, C.C., ANDRADE, G.R.S., ALMEIDA, L.E., "Biodegradação em solo simulado de compósitos de pead/pró-oxidante/ casca de arroz: aplicação em tubetes agrícolas", *Revista Matéria*, v. 23, n. 4, pp. e12264, 2018. doi: http://doi.org/10.1590/s1517-707620180004.0598.

[35] ASAITHAMBI, V., CHANDRASEKAR, M.S., "Experimental investigation on development and machinability of copper matrix hybrid composite – graphene and SiC / TiC / ZrO2 / AlMg reinforcements", *Matéria,* v. 30, pp. e20240837, 2025. doi: http://doi.org/10.1590/1517-7076-rmat-2024-0837.

[36] FERREIRA, A.S., LOPES, F.P.D., MONTEIRO, S.N., *et al*., "Charpy impact resistance of alkali treated curaua reinforced polyester composites", *Matéria,* v. 15, n. 2, pp. 132–139, 2010. doi: http://doi.org/10.1590/S1517-70762010000200007.

[37] SANTAFÉ JÚNIOR, H.P.G., LOPES, F.P.D., COSTA, L.L., *et al*., "Mechanical properties of tensile tested coir fiber reinforced polyester composites", *Revista Materia*, v. 15, n. 2, pp. 113–118, 2010.

[38] FERREIRA, A.S., NASCIMENTO, D.C.O., MONTEIRO, S.N., "Izod impact energy study of re-forced polisher matrix compounds with curaous fibers aligned and epoxy matrix reinforced with piassava fibers", *Matéria,* v. 23, n. 4, pp. e12238, 2018. doi: http://doi.org/10.1590/s1517-707620180004.0572.

[39] PALANISAMY, S., PALANISAMI, K., MADESHWAREN, V., "Nano iron particles influence on mechanical properties and morphological analysis of polymer composites", *Matéria,* v. 30, pp. e20240698, 2025. doi: http://doi.org/10.1590/1517-7076-rmat-2024-0698.

[40] GUNES, I., UYGUNOĞLU, T., ÇELIK, A.G., "Tribological properties of fly ash blended polymer composites", *Matéria,* v. 26, n. 1, pp. e12929, 2021. doi: http://doi.org/10.1590/s1517-707620210001.1229.

[41] NATARAJAN, L.R., KATHIRESAN, S., VINAYAGAM, M., "Effect of fiber hybridization on bi-directionally oriented natural aglass fiber reinforced polymer composites", *Matéria,* v. 30, pp. e20240648, 2025. doi: http://doi.org/10.1590/1517-7076-rmat-2024-0648.

[42] VELMURUGAN, G., CHOHAN, J.S., VELUMAYIL, R., *et al*., "Driving into the future: nano graphene and silicon dioxide enriched kevlar composites for automotive applications", *Silicon*, v. 16, n. 9, pp. 3873–3890, 2024. doi: http://doi.org/10.1007/s12633-024-02977-y.

[43] HUANG, H., HUANG, M., ZHANG, W., *et al*., "Experimental study of predamaged columns strengthened by HPFL and BSP under combined load cases", *Structure and Infrastructure Engineering*, v. 17, n. 9, pp. 1210–1227, 2021. doi: http://doi.org/10.1080/15732479.2020.1801768.

[44] ABDALLA, J.A., HAWILEH, R.A., BAHURUDEEN, A., *et al*., "A comprehensive review on the use of natural fibers in cement/geopolymer concrete: A step towards sustainability", *Case Studies in Construction Materials*, v. 19, pp. e02244, 2023. doi: http://doi.org/10.1016/j.cscm.2023.e02244.

[45] BISPO, M.C., LOPES, B.H.K., FONSECA, B.C.S., *et al*., "Electromagnetic properties of carbon-graphene xerogel, graphite and ni-zn ferrite composites in polystyrene matrix in the x-band (8.2 – 12.4 ghz)", *Matéria,* v. 26, n. 2, pp. e12967, 2021. doi: http://doi.org/10.1590/s1517-707620210002.1267.

[46] AZEVEDO, J.B., VIANA, J.D., DE CARVALHO, L.H., *et al*., "Characterization of composites made from biodegradable polymer and rice husk using two processing techniques", *Matéria*, v. 21, pp. 11709, 2016. doi: http://doi.org/10.1590/S1517-707620160002.0037.

[47] SEKAR, B.K., PRADEEP, G.V.K., SILAMBARASAN, R., *et al*., "Microstructural and mechanical characterization of AA2124 aluminum alloy matrix composites reinforced with Si3 N4 particulates fabricated by powder metallurgy and high-energy ball milling", *Matéria*, v. 29, n. 3, pp. e20240196, 2024. doi: http://doi.org/10.1590/1517-7076-rmat-2024-0196.